Biophysical Journal, Volume *114*

Supplemental Information

The Structural Basis of IKs Ion-Channel Activation: Mechanistic Insights from Molecular Simulations

Smiruthi Ramasubramanian and Yoram Rudy

Supplement

The Structural Basis of IKs Ion-Channel Activation: Mechanistic Insights from Molecular Simulations

By

Smiruthi Ramasubramanian and Yoram Rudy

Table of Contents

Section 1

Structure

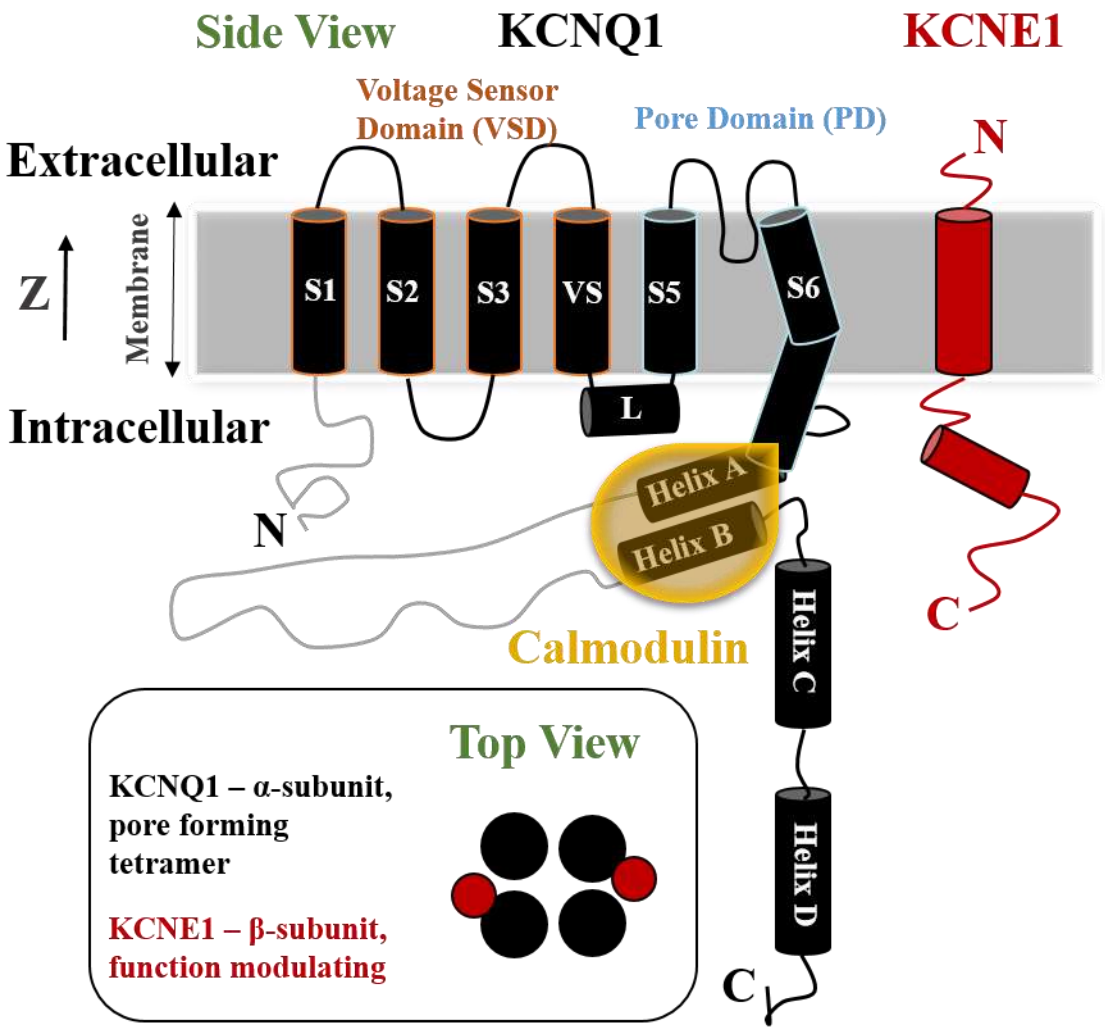

Figure S1. Schematic of KCNQ1 and KCNE1 segments. *The cylinders represent a-helices and the grey lines represent disordered protein segments that are not part of the structural model. The starting model of IKs is built based on this schema. N, C indicate the N- and C-terminus, respectively.*

** Note that in this figure and other figures of the supplement, symbols and corresponding structural elements are color-coded.*

Kv channels (voltage gated potassium ion-channels) assemble as a tetrameric structure. In the case of IKs, each of the four identical pore forming subunits (a subunits, KCNQ1) contain six transmembrane segments (S1-S6). Respectively, segments S1-S4 and S5-S6 constitute the VSD (Voltage Sensor Domain) and PD (Pore Domain). The P-loop in the PD features a selectivity filter that determines which cations pass through the pore. Accessory subunits (e.g. KCNE1, Calmodulin) modulate the function of the protein; these subunits bind and interact with different parts of the a subunits. The N-terminus of KCNQ1 (1-120 residues) and the 100 residue long linker between HelixA&B (HelixA and HelixB) are not modelled since experimental data suggest that they are disordered(1, 2). All other components of the IKs model are built using published structural data from experiments. In this paper, IKs refers to a Kv7.1 homogeneous pore forming tetramer with two KCNE1 subunits, positioned as shown in the top view

(A)

```
3LUT        ---CERVVINISGLRFETQLKTLAQFPETLLGDPKKRMRYFDPLRNEYFFDRNRPSFDAI
3LNM        HESSERVVINISGLRFETQLKTLAQFPETLLGDPKKRMRYFDPLRNEYFFDRNRPSFDAI
KCNQ1TM     ----------------------------------------HVQGRVYNFLERPTGWKCF
                                                     .   . * * ..  .:..:

3LUT        LYYYQSGGRLRRPVNVPLDIFSEEIRFYELGEEAMEMFREDEGYIKEEERPLPENEFQRQ
3LNM        LYYYQSGGRLRRPVNVPLDIFSEEIRFYELGEEAMEMFREDEGYIKEEERPLPENEFQRQ
KCNQ1TM     VYHFAVFLIVLVCLIFSVLSTIE-----------------------------------
            :*::     :   : . :    *

3LUT        VWLLFEYPESSGPARIIAIVSVMVILISIVSFCLETLPIFRDENEDMHGGGVTFHTYSQS
3LNM        VWLLFEYPESSGPARIIAIVSVMVILISIVSFCLETLPIFRDENEDMHGGGVTFHTYSQS
KCNQ1TM     ------------------------------------------------------------


3LUT        TIGYQQSTSFTDPFFIVETLCIIWFSFEFLVRFFACPSKAGFFTNIMNIIDIVAIIPYFI
3LNM        TIGYQQSTSFTDPFFIVETLCIIWWSFEFLVRFFACPSKAGFFTNIMNIIDIVAIIPYYV
KCNQ1TM     ----QYAALATGTLFWMEIVLVVFFGTEYVVRLWSAGCRSKYVGLWGRLRFARKPISIID
                * ::  *. :* :* : :::::. *::**:::. .:: :.    .:      *
                                        S4
3LUT        TLGTELAEKPEDAQQGQQAMSLAILRVIRLVRVFRIFKLSRHSKGLQILGQTLKASMREL
3LNM        TIFLTESNKSVLQFQ----NVRRVVQIFRIMRILRIFKLSRHSKGLQILGQTLKASMREL
KCNQ1TM     LIVVVASMVVLCVGSKGQVFATSAIRGIRFLQILRMLHVDRQGGTWRLLGSVVFIHRQEL
             :    :       .         :: :*::::*::::.*:.   ::**..:    :**

3LUT        GLLIFFLFIGVILFSSAVYFAEADERD----SQFPSIPDAFWWAVVSMTTVGYGDMVPTT
3LNM        GLLIFFLFIGVILFSSAVYFAEADERD----SQFPSIPDAFWWAVVSMTTVGYGDMVPTT
KCNQ1TM     ITTLYIGFLGLIFSSYFVYLAEKDAVNESGRVEFGSYADALWWGVVTVTTIGYGDKVPQT
               ::: *:*:*: *  **:** *  :     :* *  **:**.**::**:**** ** *
                                  S6
3LUT        IGGKIVGSLCAIAGVLTIALPVPVIVSNFNYFYHRE---TCERVVINISGLRFETQLKTL
3LNM        IGGKIVGSLCAIAGVLTIALPVPVIVSNFNYFYHRETHESSERVVINISGLRFETQLKTL
KCNQ1TM     WVGKTIASCFSVFAISFFALPAGILGSGFALKVQQKQRQ--------------------
              ** :.*  :: .:  :***. :: *.*    :::
```

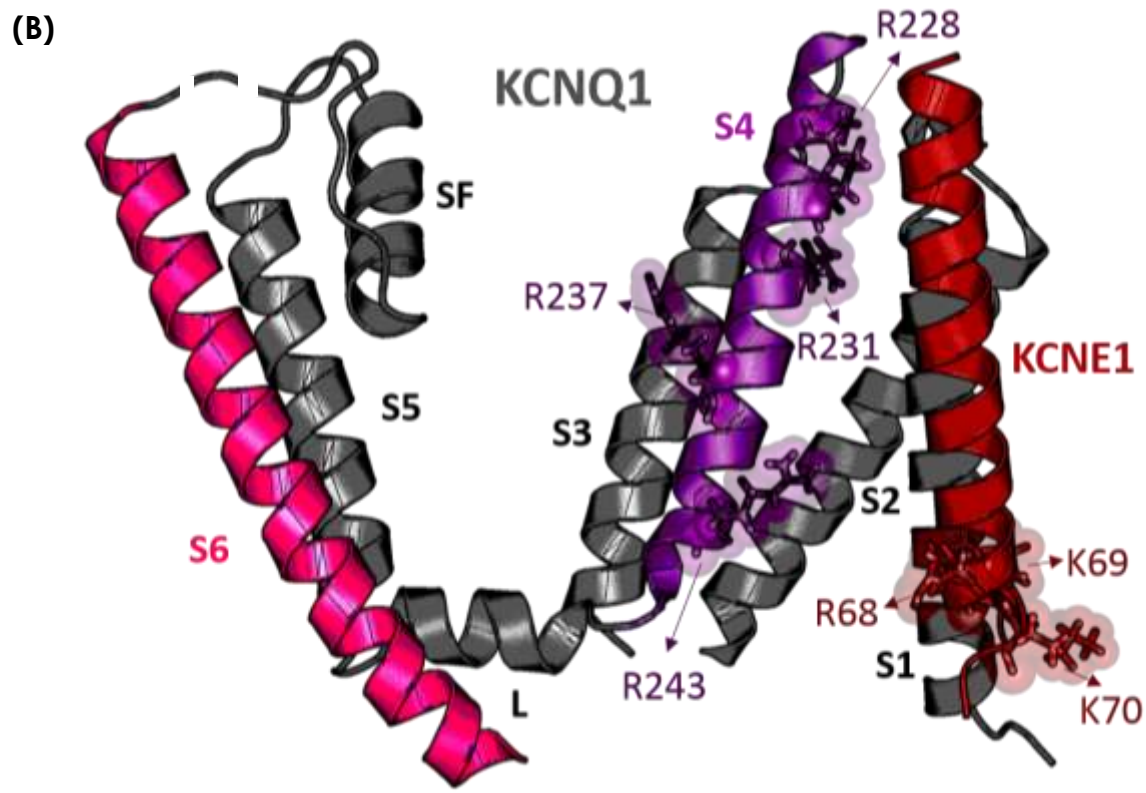

Figure S2. Homology model of KCNQ1 (homologous to Kv1.2/2.1) docked with NMR determined KCNE1 structure. *(A) Sequence alignment of KCNQ1 transmembrane domain with Kv1.2 (RSCB: 3LUT) and Kv1.2/2.1 (RSCB: 3LNM). S4 and S6 segments are highlighted, to correspond with panel B. (B) The resultant model of transmembrane KCNQ1-KCNE1 is shown, with important segments and charged residues that play a vital role in gating highlighted. Note that long linkers (S2-S3 and SF-S6) are not shown to provide better figure clarity. (L, S4-S5 linker; SF, selectivity filter; KCNQ1, a-subunit of IKs; KCNE1, β-subunit of IKs)*

Experimental structural data for KCNQ1 were not available at the inception of this project. Therefore, we applied homology modelling using Kv1.2

crystal structure data (3–5) to build the KCNQ1 transmembrane domain (previously published (6, 7)). Furthermore, Kv1.2/2.1 chimera crystal structure (8) was utilized to remedy any poor resolution segments of the Kv1.2 crystal structure and also fill in gaps of the aligned sequence (Figure S2A). This information along with attributes from previously published computational models (9) were incorporated in building the homology model of the KCNQ1 pore forming tetramer. The structure was further optimized using the Rosetta software (connecting loops and linkers) (10). Many conformations similar to the recently published experimental KCNQ1 structure (11) were sampled in the constructed IKs structure library (details in Section 2 and Figure S11).

The KCNE1 transmembrane helix is important for the functional modulation of the KCNQ1 tetramer. It is responsible for slowed activation and increased magnitude of current (12). Human KCNE1 structure has been determined using NMR (13–16). Many experimentally determined KCNQ1-KCNE1 interaction sites and structural models of KCNE1 docking have been published (3, 5). Rosetta FlexPepDock refinement protocol was used to further optimize the transmembrane interface between KCNQ1 and KCNE1 (17). Recently published KCNQ1/KCNE1 docking data show consistent results (18).

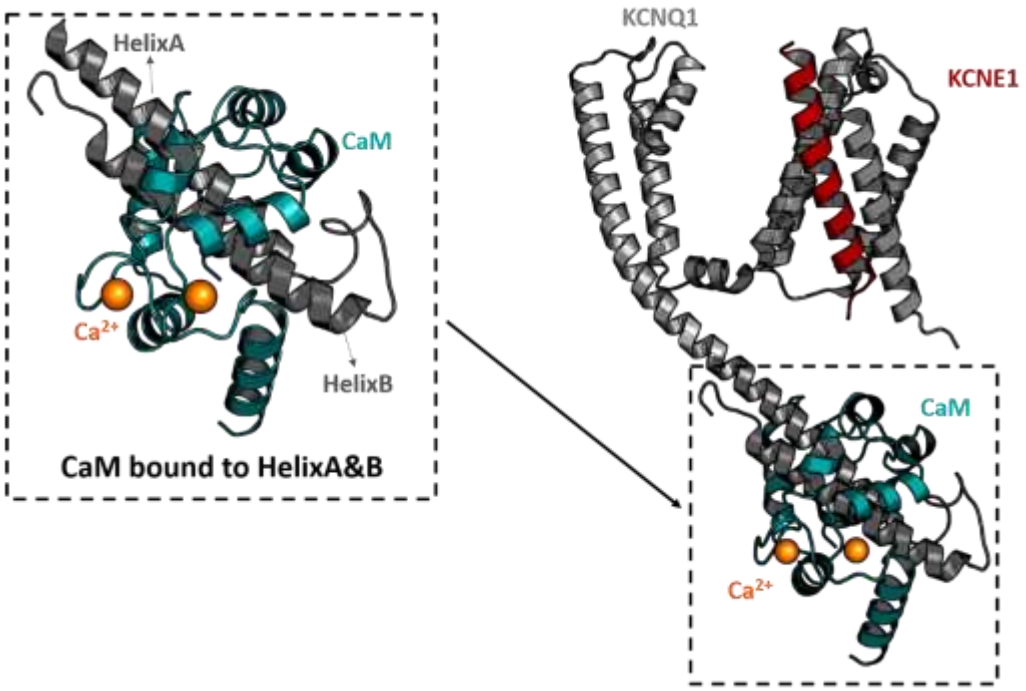

Figure S3. Incorporating CaM interactions with IKs. *The resultant structure after stitching together the transmembrane IKs complex and the crystal structure of HelixA&B is shown. The latter is bound to CaM with two Ca^{2+} ions (dashed box)* (19). *(CaM, Apo-calmodulin; Ca^{2+}, calcium ions; HelixA&B,* HelixA and HelixB*)*

Calmodulin is essential for channel assembly and gating; it mediates Ca^{2+} sensitive modulation of the IKs ion-channel (20–22). Mutations in calmodulin can disrupt current and the current-voltage relationship. Note that calmodulin in this section refers to Apo-calmodulin (a variant bound to 2 as opposed to 4 Ca^{2+} ions; CaM). This is the only calmodulin variant for which experimentally-determined structure was available, in the context of IKs ion-channels, when the protein structure was constructed.

Rosetta was used to minimize steric clashes of side-chains and extend S6 to HelixA using secondary-structure predictions of S6-HelixA amino acid sequence by the DSSP algorithm (23, 24). The latter is consistent with the ridged-lever arm attached to CaM near the proximal membrane region, as suggested by small-angle X-ray scattering data (19). Experimental observations also suggest that each HelixA and HelixB (HelixA&B) of individual KCNQ1 segment binds to CaM. Thus the complete IKs ion-channel model has a CaM bound to each KCNQ1 segment (4 KCNQ1: 4 CaM).

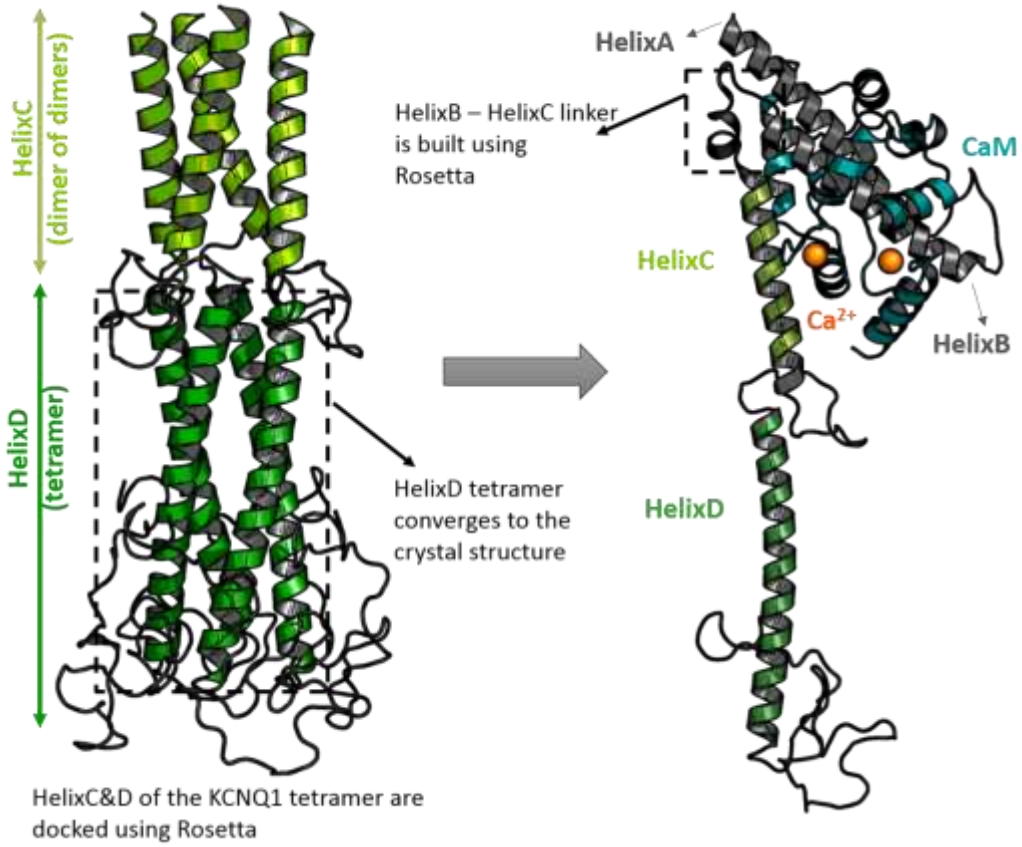

Figure S4. Rosetta docked model of HelixC&D. *HelixD tetramer of the docked model shows convergence to the published crystal structure. HelixC&D is connected to the HelixA&B model bound to CaM by a ten residue linker (built using Rosetta). (CaM, Apo-calmodulin; HelixA&B,* HelixA and HelixB; *HelixC&D, HelixC and HelixD)*

HelixC and HelixD (HelixC&D) secondary structure and interactions between these segments in the KCNQ1 tetramer have been investigated using experimental techniques such as CD spectroscopy and crystallography(1, 2, 25).

Using this information with the Rosetta module (26), HelixC&D segments of the KCNQ1 tetramer were docked and minimized for steric clashes. The resulting simulated HelixD tetramer shows convergence with its resolved crystal structure (2); RMSD comparison between the backbone atoms of the model and crystal structure is less than 0.13 Å. The linker between HelixC&D and HelixA&B of each segment is built using Rosetta to complete the C-terminus of the KCNQ1 tetramer.

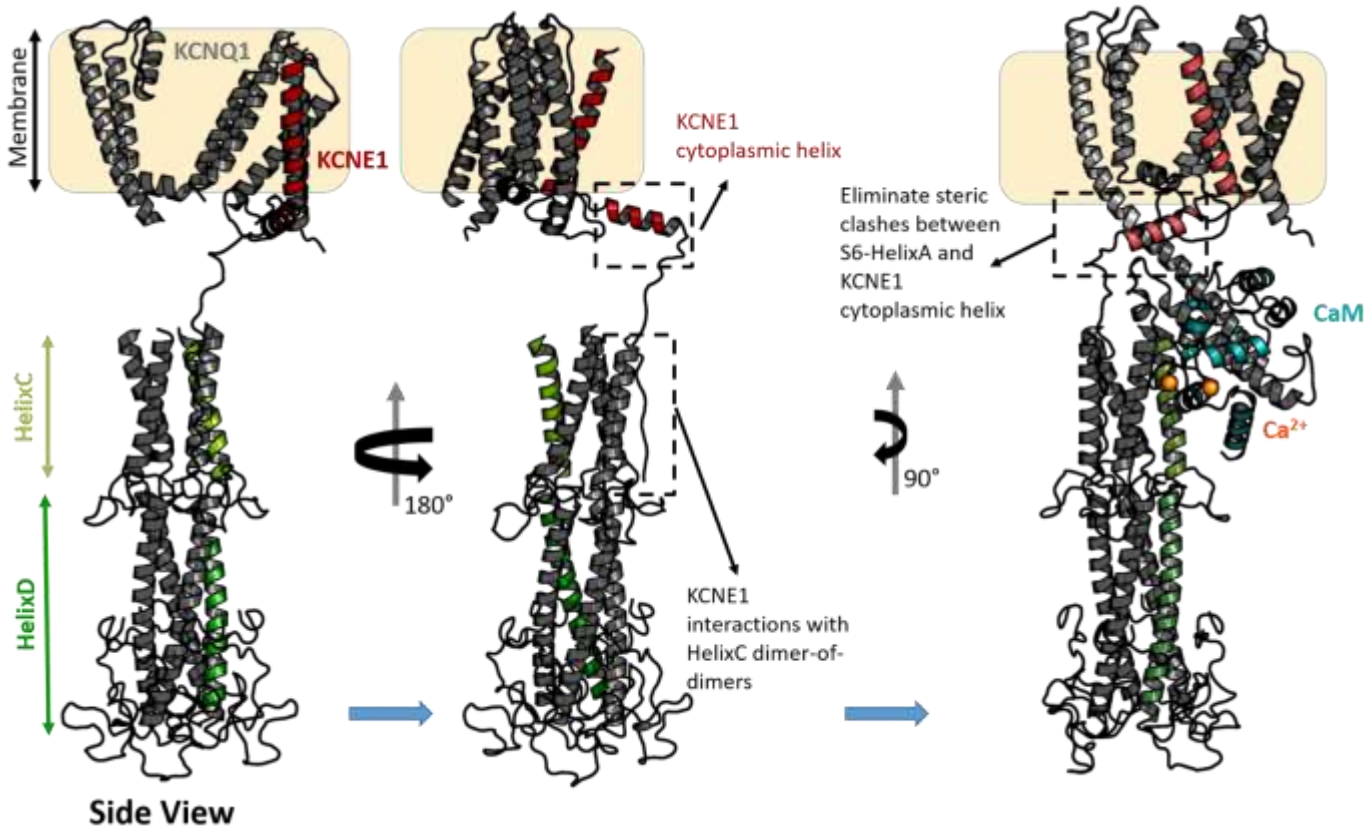

Figure S5. Side view of KCNQ1-KCNE1 interaction sites. *KCNE1 cytoplasmic interactions with HelixC dimer-of-dimers is resolved using Rosetta. The position of the cytoplasmic KCNE1 helix is adjusted to remove steric clashes and the linkers between KCNE1 C-terminus tail, KCNE1 cytoplasmic helix and KCNE1 transmembrane helix are built using Rosetta. Dashed-boxes and arrows represent interaction interfaces between KCNQ1 and KNCE1 in the cytoplasmic region.*

Rate dependent facilitation of IKs depends on the KCNE1 C-terminal interactions with KCNQ1 C-terminus (27). Mutations in the C-terminus region of

KCNE1 can produce defective rate dependence and thus cause arrhythmias (27). KCNE1 NMR data show a secondary helical segment, which is most likely in the cytoplasm (14, 15). Additionally, experiments have shown the C-terminal segment of KCNE1 interacts with the KCNQ1 HelixC coiled coil (1). This interaction is at the interface between two KCNQ1 segments and was resolved using the Rosetta module (17, 28). The linkers between the KCNE1 helical segments and C-terminal interaction site are also built using Rosetta. The KCNE1 cytoplasmic helix is adjusted to remove steric clashes (against S6-HelixA).

The IKs tetramer structure was minimized using MODELLER (29) (10,000 steps, interaction energy is minimized). Although the stoichiometry of KCNQ1:KCNE1 ratio is controversial, the expression levels in cardiac myocytes suggest at least a 4:2 ratio (30–34). Thus, two KCNE1 β-subunits were docked to the KCNQ1 tetramer (on opposite KCNQ1 subunit clefts).

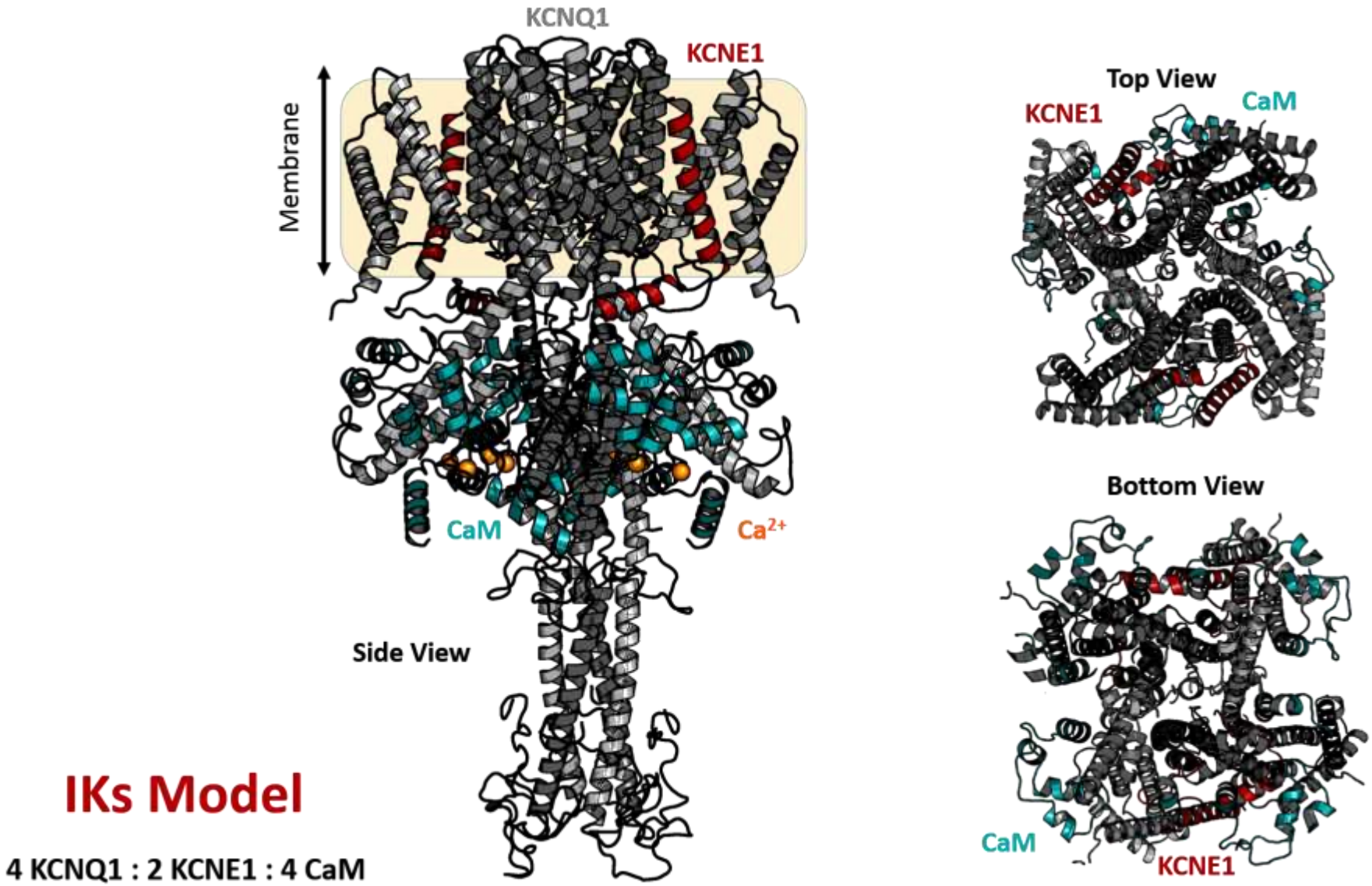

Figure S6. The complete structural model of *IKs. Side, Top and Bottom views*

Section 2

Methodology

Introduction

It is extremely challenging to computationally simulate the dynamics of large proteins such as ion-channels, in the milliseconds to seconds timescale that is necessary to study their physiological function, e.g. channel gating. The entire space of trajectories of protein conformational changes needs to be assessed in order to meaningfully understand the relationship between structure and physiological function. To achieve this, all possible conformations of the protein need to be constructed. This is an impossible task with a large protein such as the IKs ion-channel; the backbone of each amino acid has two rotational degrees of freedom (phi, psi) and its respective side chains include additional degrees of freedom. Even with a simplified structure, the IKs ion-channel has a total of 4836 degrees of freedom (2418 residues, without including sidechain degrees of freedom). When assessed with a coarse grain grid (phi and psi range [-180°, 180°], step 10°), this results in 1296^{4836} possible conformations during dynamics. Even if this computation were possible, the stratagem of using a coarse grid would reduce the structural resolution of the model and result in invalid physiological interpretations. Thus, a more economical approach is required to generate a library of conformations in a fine-grain grid and to estimate the respective structural energy for simulating dynamics. The outline for the approach developed and used in this study is detailed in Figure S7; the following sections provide the relevant details.

2.1: Sampling the IKs Gating Conformational Space and Energy Calculations

Generating a library of conformations for simulating ion-channel gating

From Experimental data, it is known that during gating (dynamics of the ion-channel in response to changes in membrane voltage (V_m)) the voltage sensor (VS, S4 transmembrane helix with positively charged residues) moves along with the S4-S5 linker (S4S5L), resulting in conformational changes of the pore (35–40). During membrane depolarization, VS moves upward (outward) towards the extracellular domain; it moves down (inward) during repolarization (Figure S8). This movement of VS can be characterized with 6 degrees of freedom (Figure S9).

In order to build a library of conformations that best represent the structural changes of the ion-channel during gating, VS of each segment in the KCNQ1 tetramer (Figure 1 in main text) was perturbed (translation and rotation with a resolution of 0.25Å and 0.1rad, respectively) in the dimensions shown in Figure S9. Experimental constraints (3, 41–48) were checked to ensure that the VS conformational change is physiologically possible. Next, the broken linkers between S3-S4 and S4-S5 were rebuilt (with Rosetta (49); the S4S5L is allowed to move within 0.25Å and 0.1rad) to accommodate this change in the VS conformation. Any steric clashes were eliminated and total energy of the protein was minimized (MODELLER (29); the backbone atoms of the VS were constrained to the new position). A representative schema of the aforementioned process is shown in Figure S10.

The electrostatic energy of the protein was calculated using Adaptive Poisson-Boltzmann Solver (APBS, APBSmem (50–54)) for different V_m. The membrane thickness was assumed to be 30Å (including 4Å ester headgroup of the lipid) and the dielectric of the protein, membrane, lipid headgroup and water used to calculate the energy was 2, 2, 80 and 80, respectively. Since the total energy of the protein has been minimized, only the electrostatic energy component of the total energy changes in response to changing V_m. The 3D coordinates of the protein structure and its electrostatic energy are tabulated at the end of each VS conformational change for different V_m.

To ensure that the conformational space of VS was searched effectively and efficiently, a rapidly-exploring tree algorithm is used (55–59). At each iteration, a new conformation is sampled at random and if this conformation meets the experimental constraints, a node is attached to the tree and the process continues. The probability that a node will be chosen for expansion depends on the volume of the unexplored region in the proximity of the node and consequently the tree will rapidly grow in unexplored regions of the conformational space. Assumptions used while building the library include: the backbone of secondary structures of the protein (helices and beta sheets) are considered to be rigid. Membrane and water/ions are considered implicit during energy calculations.

Previous papers have reported conformational libraries of the KCNQ1 tetramer (6, 7, 60). However, this library is unique in that it ***does not*** assume

(1) Movement of the 4 VS in the tetramer is symmetric,

(2) S3 and S4 move together ("paddle motion"(61, 62))

(3) Immobility of "static" segments (other than S3-S4, S4S5L and S6; both backbone and side chain)

(4) Mechanical coupling between VS and S6 via S4S5L - i.e. higher Z position of S4 results in wider pore.

(5) Allosteric gating mechanism - i.e. all 4 VS segments have to be in a relatively high Z position in order for the pore to open ("cooperativity").

Additionally, this library includes the complete structure of IKs, modelled with the available experimental data (refer to Supplement Section 1). The structure was not constrained with any non-physiological parameters e.g. application of extremely high V_m. Furthermore, the degrees of freedom of the entire structure were not limited or reduced and were allowed to change in response to the perturbed VS conformation.

Note that the 'pore diameter' is measured as the minimum distance between side-chain residues at the activation gate of the pore (63). Although the IKs pore does not have the 'PVP' (proline-valine-proline) kink in the S6 segment like Kv1.2, it does have a 'PAG' (proline-alanine-glycine) motif that results in a gradual bend. Nevertheless, the activation gate is assumed to be in the same region of S6 (below the cavity, in the interface between the membrane and cytoplasmic region).

The library of conformations were built before the recent KCNQ1 cryo-electron microscope (cryo-EM) experimental data (RSCB: 5VMS, (11)) was made available.

Therefore, this new structural data served to validate the extensive *de novo* sampling by our structure library of the IKs conformational space. The library samples many conformations similar to the cryo-EM structure (chain A, transmembrane segment) and one such conformation with the smallest small root-mean-squared error (RMSE; comparing backbone atoms) to 5VMS is shown in Figure S11. The largest backbone fluctuations occur at linker positions and the S1, S2, S5, P-loop and SF show very small fluctuations. Thus, the library is able to sample all possible conformations of the IKs gating space, including a possible (experimentally determined) KCNQ1 conformation.

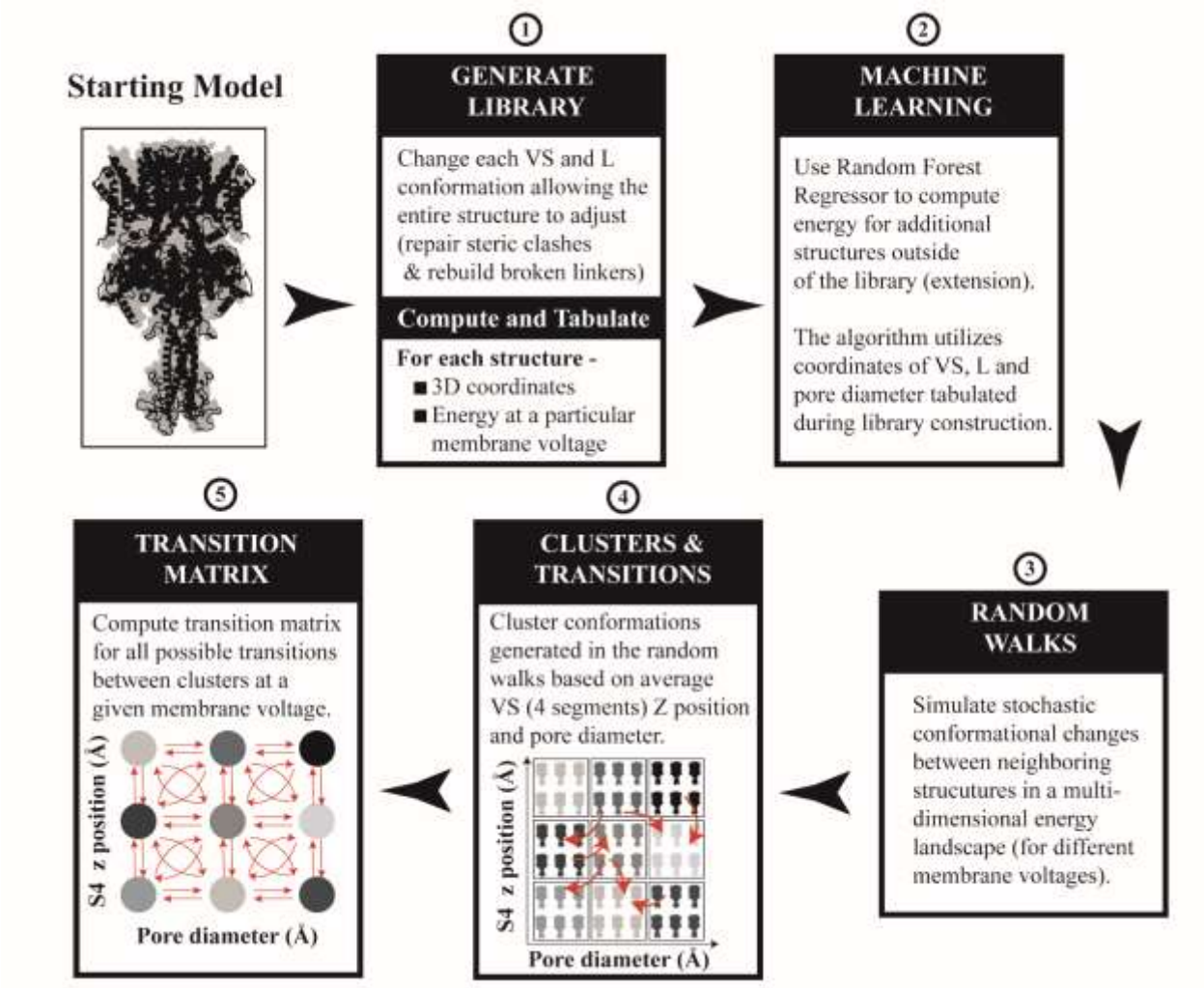

Figure S7. A flow chart for simulating protein dynamics.

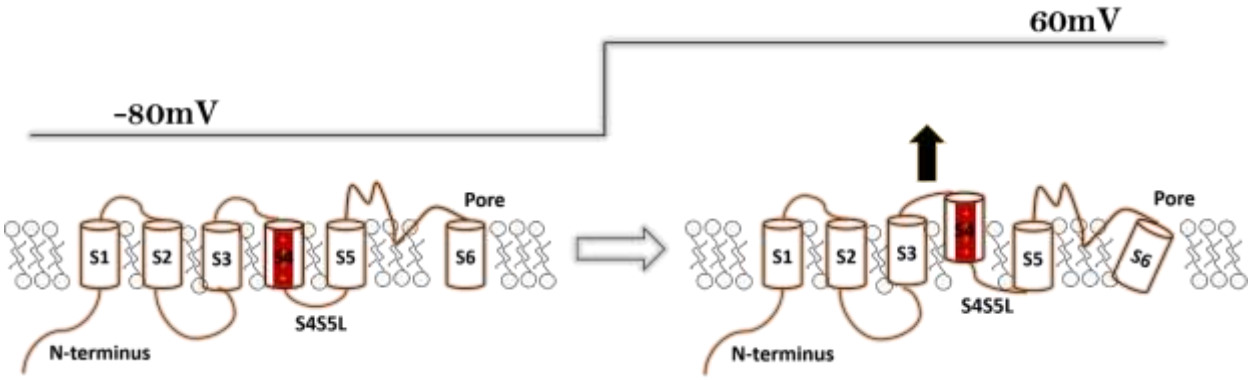

Figure S8. A cartoon representing the upward/outward motion of VS (S4) during depolarization. *The VS moves towards the extracellular side of the membrane in the Z-direction (perpendicular to the membrane) with some rotation. The S4S5L and S6 also move to accommodate this change. (VS, Voltage Sensor; S4S5L, S4-S5 linker)*

Range of Movement

X	Y	Z
[-10,10] Å	[-10,10] Å	[-20,20] Å

Pitch	Roll	Twist
[-π,π) rad	[-π,π) rad	[-π,π) rad

Resolution

X,Y,Z	Rotation
0.25 Å	0.1 rad

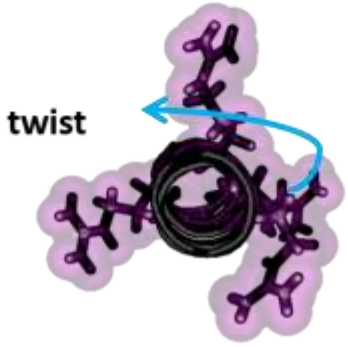

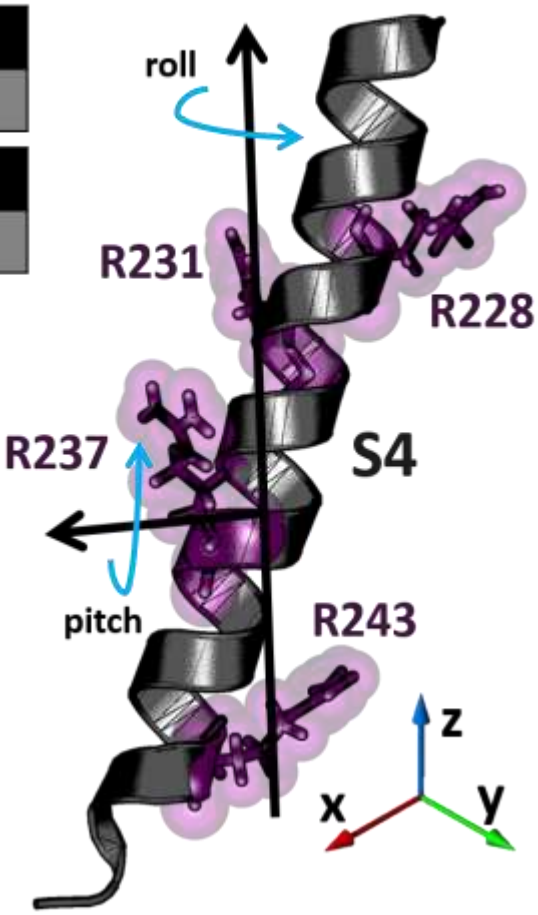

Figure S9. Degrees of freedom of Voltage Sensor (VS). *The VS is translated and rotated in X, Y, Z and pitch, roll and twist dimensions. The translation and rotation resolution is 0.25Å and 0.1rad, respectively. Positively charged arginine residues are identified (purple). (VS, Voltage Sensor (S4))*

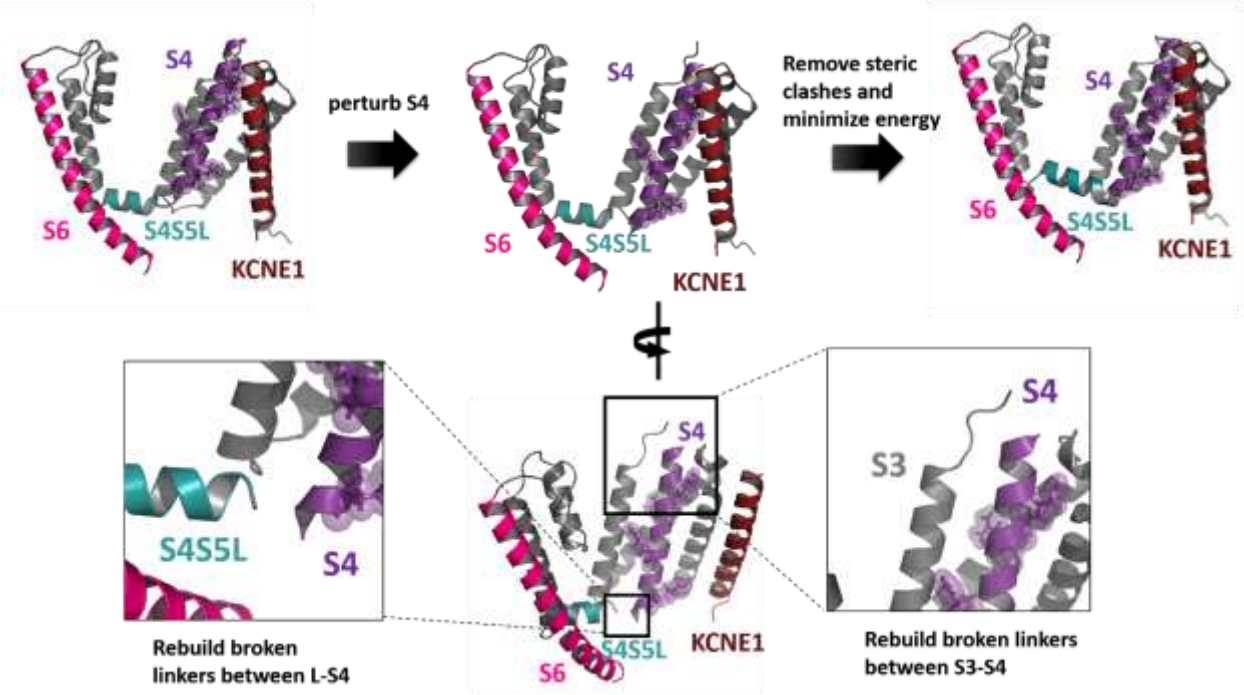

Figure S10. Perturbing VS (S4) and rebuilding structure. *The figure shows a schema going from the starting structure to the final minimized conformation. Steps include perturbing VS, rebuilding broken linkers, removing steric clashes and minimizing the total energy of the protein. Note that the VS arginine residues (R228, R231, R237, R243) are marked as sticks to show rotation (refer to Figure S8). (VS, Voltage Sensor (S4); S4S5L, S4-S5 linker; KCNQ1, α-subunit of IKs; KCNE1, β-subunit of IKs)*

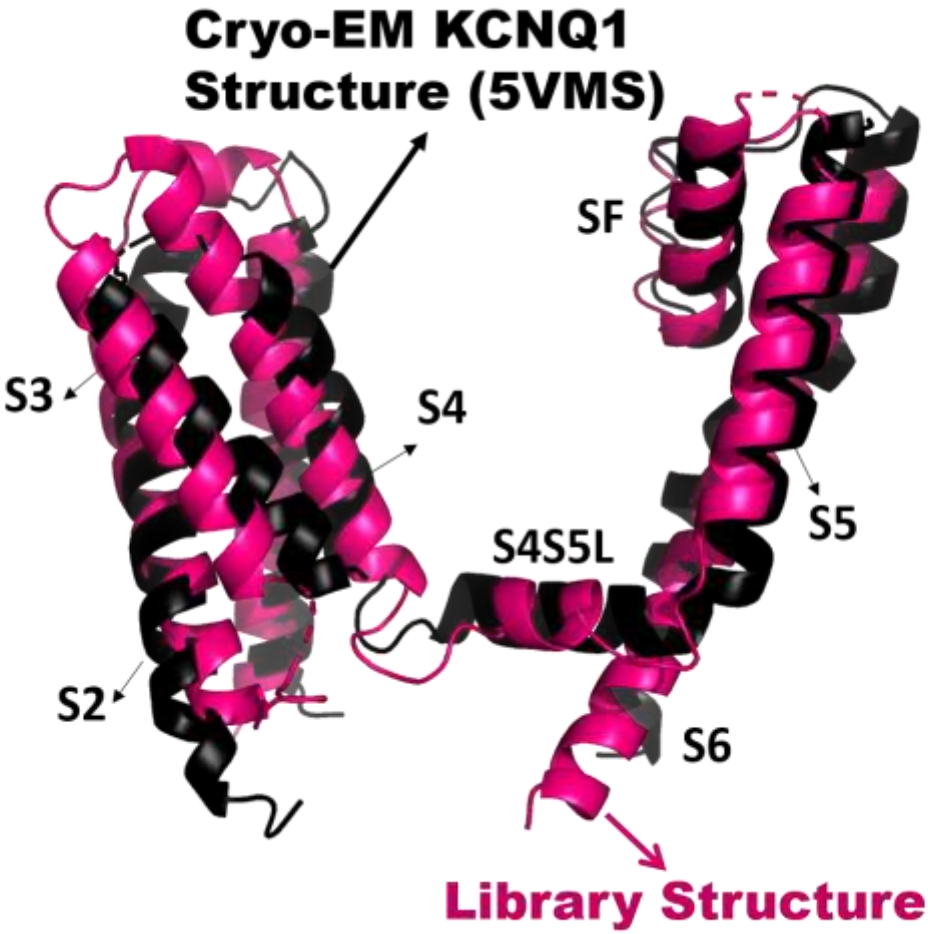

Figure S11. Comparison of 5VMS cryo-electron microscope KCNQ1 (chain A) structure to a library conformation. *The library conformation (118T-358K; pink) with the smallest backbone root-mean-squared error of 0.92Å aligned with 5VMS (108T-348K; black). The 5VMS transmembrane segments are labelled S1-S6. Note that long flexible linkers (S2-S3 and Ploop-S6) are omitted from this calculation.*

Energy calculations

The non-electrostatic energy components of the total protein energy were calculated with NAMD Energy plugin (with VMD (64, 65)) and the electrostatic energy was calculated using ABPSmem using CHARMM parameters (50, 52, 66) (at different V_m). APBS (67) is a well-established and tested computation method to calculate electrostatic energy of proteins as precisely as possible using implicit dielectrics. Multiple levels of field focusing were considered in these calculations by iteratively computing protein electrostatics with a coarse grid followed by similar calculations on a finer grid with boundary conditions determined from the former (coarse) run. A set of conformations are chosen randomly from the library and energy statistics (mean and standard deviation) were calculated. More conformations from the library were added iteratively to the latter set until the difference of consecutive calculation was less than 1%. Energy components of the protein (of randomly chosen 571,775 unique conformations from the library) show that the electrostatic energy contributes most to the total protein energy (Figure S12). The energy difference of the aforementioned conformation set at different V_m (-80mV and 60mV) show that the electrostatic energy changes are large (Figure S13). Therefore, the electrostatic energy contributes most to changes in protein energy that depend on V_m. In contrast, energy components other than electrostatic energy do not change with V_m and contributed much less to the total protein energy and thus are not utilized to calculate IKs gating dynamics.

Please note that henceforth all references to energy refer to the electrostatic energy calculated using APBS, unless explicitly stated otherwise. Additionally, total

protein energy in this subsection was computed as the sum of conformational and non-bonded energies (i.e. bond, angle, dihedral, improper, van der Waal, and APBS electrostatic energies).

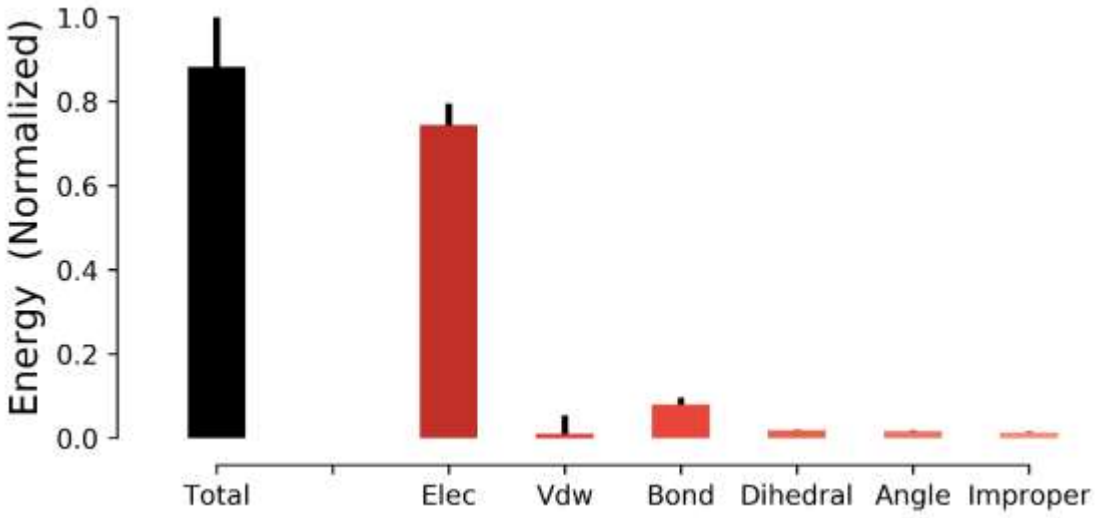

Figure S12. Energy components (normalized to total energy). *Protein energy calculated at 0mV shows that the electrostatic energy contributes ~85.5% of total energy of the protein. The bar plot shows the mean and standard deviation of 571,775 randomly chosen library conformations. NAMD Energy plugin (with VMD (64, 65)) was used to calculate non-electrostatic energy components of IKs conformational energy. APBSmem was used to calculate electrostatic energy. (Elec, electrostatic; Vdw, van der Waals)*

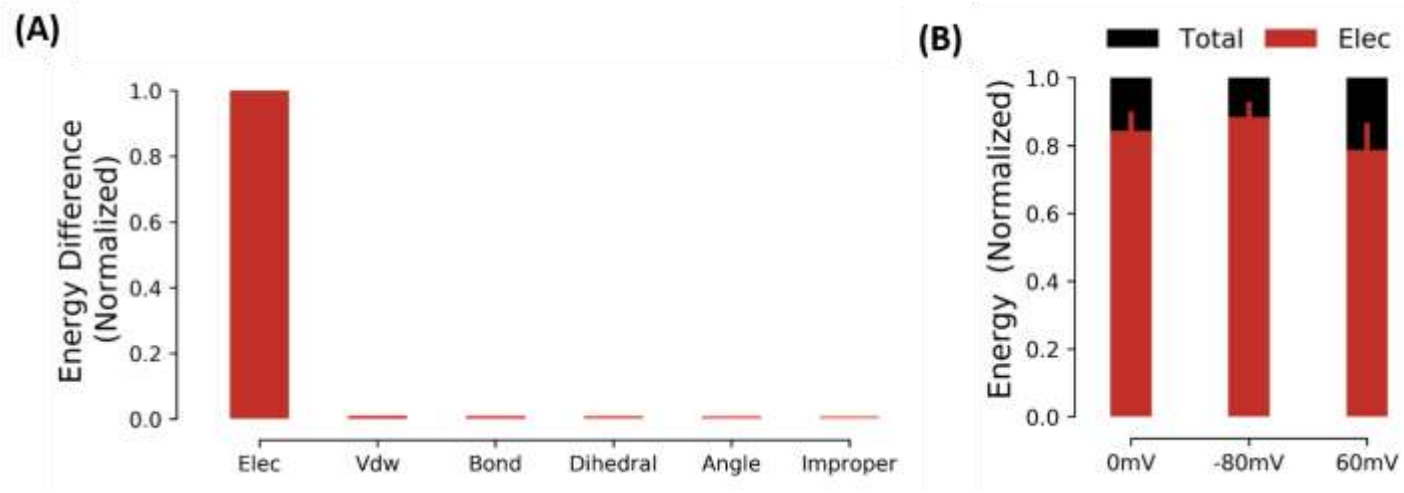

Figure S13. Electrostatic Energy contributes over 75% to total protein energy even at different membrane voltages. *(A) Mean energy difference of protein structures at V_m -80mV and 60mV. The data are normalized to the electrostatic energy difference and relative ratios show that electrostatic energy contributes most to IKs conformational energy changes that depend on V_m. (B) The relative ratios of electrostatic energy to total energy at V_m of 0mV, -80mV and 60mV. The electrostatic energy contribution is shown to be dominant over a range of physiological V_m. Note that the library structures used in this analysis were the same as in Figure S12. (V_m, membrane voltage; Elec, electrostatic; Vdw, van der Waals)*

2.2: Application of Machine Learning for Constructing the Protein Energy Landscape

Although the generated library of conformations is extensive and examines many degrees of freedom, it does not contain all possible conformations required to construct the ion-channel energy landscape during gating. A novel aspect of this study is the prediction of structural energy using Machine Learning (ML) algorithm. Using conformational features obtained from the protein 3D coordinates (tabulated from the library; section 1), The ML algorithm can compute energy of structures outside the library and thus enable the required extensive exploration of the energy landscape.

Choosing features to train the ML Algorithm

The structural energy to be predicted depends on the placement of charged atoms in the protein conformations. The majority of atoms position change occurs at the VS and S4S5L segments of the tetramer (refer to Section 1). Position changes of atoms in other segments are smaller (0.1-0.6Å) and contribute little to the change in energy (except S6, HelixA and Calmodulin; but most of these segments are in the cytoplasm and thus shielded from the transmembrane segments). Therefore, using the 6 dimensions of VS and S4S5L (48 dimensions in the tetramer) as features for training the ML algorithm to predict energy was expected to be an effective strategy. The same set of features was also suitable for training the ML algorithm to predict the

diameter of the pore during a random walk, as changes in these features result in altered pore conformations.

ML: The random forest algorithm

The random forest algorithm (68) is an estimator that fits varying branches of decision trees with varying sub-samples of the training data. An extended tree regression algorithm with 2500 trees (69, 70) was used to predict the structural energy of a conformation given its VS and S4S5L features. To train and implement the ML, the library was divided into training and testing sets with no overlaps. The ML is "trained" recursively with the training set and uses averaging to prevent over-fitting. When the regression algorithm works, it will predict the energy of the test set of structures with minimum error (Figure S14).

The features extracted from the structural library were pre-processed with Principal Component Analysis (PCA; (71–73) and the energy values were scaled between [-1, 1] to increase the accuracy of the ML. PCA showed that all 48 features of the protein were important to completely represent the conformation. Also, 1.5 to 3 million structures were required to train the ML to predict the energy with acceptable accuracy (Figure S14.A). Using this technique, the libraries of IKs structures were trained with ML to predict their structural energy (Figure S14.B).

The MSE (Mean Squared Error) is calculated between the predicted and the actual energy values (recorded in the library) for corresponding testing structures not used to train the ML. The MSE decreases with increased size of the training set. The

convergence ensures that the ML can predict the energy of structures outside the library with acceptable accuracy. A similar technique was used predict the pore diameter of a structure; it also showed similar convergence with 3 million structures in the library.

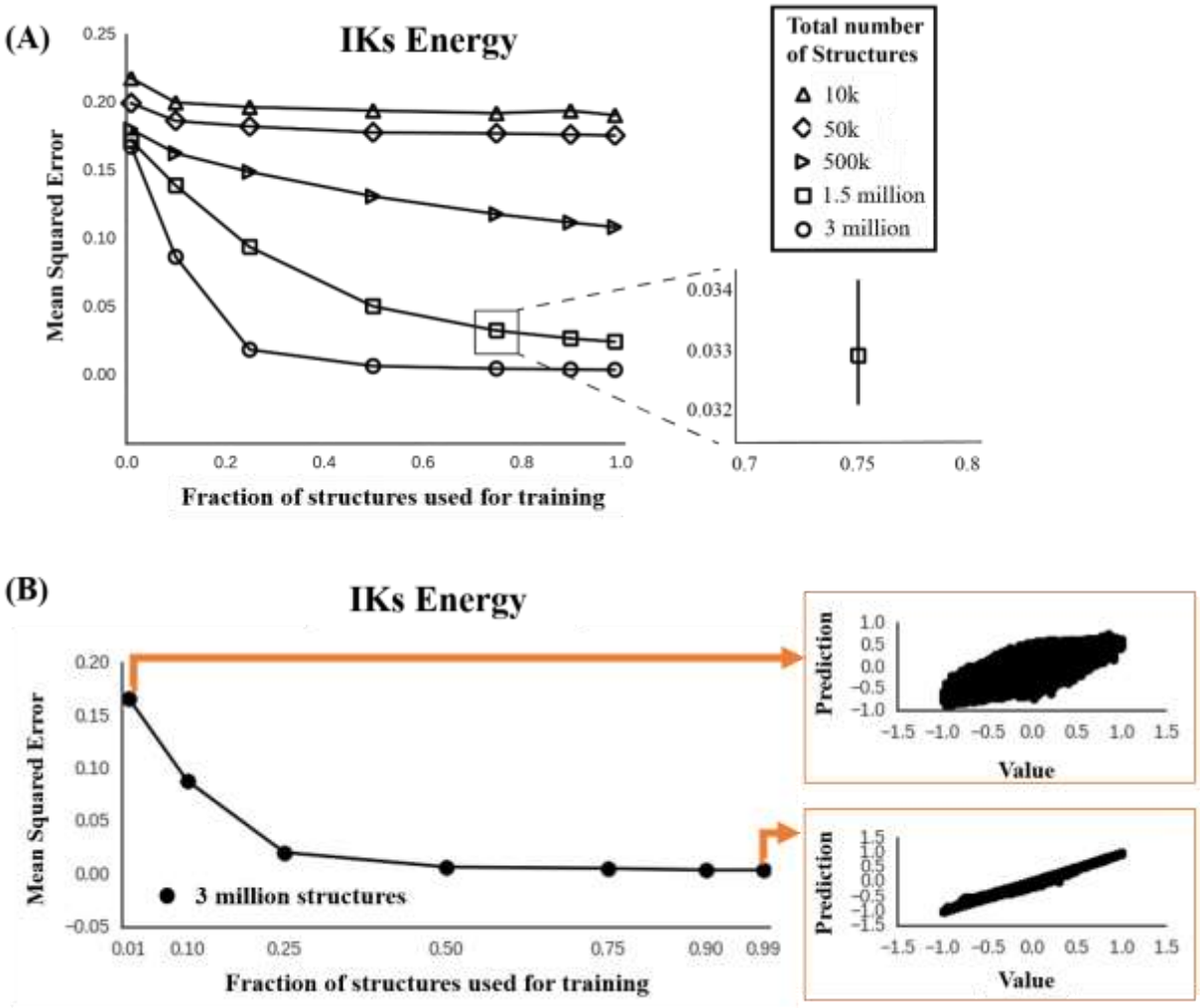

Figure S14. Training the Machine Learning algorithm (ML). *(**A**)The fraction of total structures (from the library) plotted against the Mean Squared Error (MSE) shows convergence with increased size of the training set. Excellent convergence is obtained with 50% and even 25% of the structures in the training set from a total of 3 million structures in the library. The inset shows zoomed in MSE with error bars (library of 1.5 million structures, 10 runs) (**B**, left) Similar plot to Panel A. (B, right) The ML predicted energy values plotted against the actual energy values from the library using a training*

set of 1% (top) and 99% (bottom) structures (randomly chosen from library). (MSE, Mean Squared Error; ML, Machine Learning)

2.3: Random walks, conformational clusters and building a structure-based Markov Model

Since the energy landscape of the protein at a particular V_m is of high dimension, it is impossible to search and visualize energy barriers and minima by observation. Random walks (stochastic structural changes based on chosen features) with different starting points on the energy landscape using the Metropolis-Hastings criterion (74, 75) provides a quantitative probability of transitions between different regions of the energy landscape. The latter approach also negates the need to calculate the partition function which would otherwise require the calculation of all possible transitions on the energy landscape. Thus, thirty random walks were simulated for 500,000 steps at different V_m and the resulting trajectories were recorded for further analysis

Clustering the structures that were visited in the random walks in dimensions of interest and physiological relevance (average VS Z position and pore diameter) further reduces the dimensions for visualization and analysis. By counting the transitions between different clusters from the random walks transition rates can be estimated (76). The resulting transition matrix was used to calculate structural changes of the protein given a particular V_m. Note that the structural clusters constitute Markov states in a Markov Model with transition rates between the states represented by the transition matrix.

Also note that the analysis was performed with structures clustered on an evenly spaced 45 by 9 grid in the pore diameter and average VS Z position dimensions (a total of 405 clusters). Note that additional features of protein structure could be included in the ML training in order to study other structure-function mechanisms.

2.4: Gating Mechanism Calculations

Gating charge calculation

The displaced gating charge was calculated using Adaptive Poisson-Boltzmann Solver (50); likely conformations of the IKs at holding potential and various steady-state depolarizing V_m were utilized in these computations. A likely IKs conformation in this computation was chosen based on its probability of being visited at a particular V_m.

Sequential Gating Analysis

The structures were alternatively clustered based on the movement of the four individual S4 segments in the Z-direction and movement of the pore. This results in a five-dimensional Markov chain (four S4 Z and one PD). Note that the SC of the control structures were re-estimated for the different clustering in this section and were utilized with the various suppressed S4 segment models. The individual S4 Z translation was segmented into 4 equally spaced clusters (between -15Å and 15Å) and the PD was discretized to 6 levels (level 0 was considered to be closed pore and levels 1-5 open pores with varying SC), resulting in 1536 structure clusters. Each cluster had a unique combination of the 5 dimensions (four S4 Z and one PD). To simulate function, movements of individual S4 in the Z-direction were incrementally suppressed (not

allowed to move during random walk simulations) and transition rates were used to construct the corresponding Markov model.

Residue pair interaction calculations

Residue interaction calculations were used to ascertain the important residue interactions that contribute to dynamics during IKs gating. Positively and negatively charged residues contribute more to the total electrostatic energy of the protein than neutral residues. Thus, important charged residues interactions that contribute to iCh gating were identified using an *in silico* residue charge neutralization method. For example, APBS was used to obtain the contribution of a residue of interest, say Residue A, to the protein electrostatic energy. Additionally, the residue's interaction strength to other residues was calculated, for example, to Residue B. The interaction between Residue A&B was obtained by neutralizing Residue B (setting the charge to zero) and recalculating Residue A's contribution to the protein energy. The difference was recorded as the 'interaction energy' between Residue A and Residue B at a certain S4 Z position and membrane voltage (60mV). Residue A's contribution to protein stabilization (a measure of interaction favorability) is also an important measure for assessing the importance of its interactions with other residues. Therefore, simultaneous assessment of the strength of the interactions and contribution to protein stabilization is provided for residues in the VS domain positioned far away and close to the KCNE1 transmembrane segment.

Section 3

Results

Introduction

Using IKs single-channel experiments (77) and pore electrostatic profile (main text, Figure 2B), a subconductance (SC) were assigned to each structure cluster modelled from a library of possible gating conformations. These calculated SC are used to simulate functional properties of the IKs model. In this section, additional single-channel statistics are shown for discreet SC levels. Supplementary analysis and simulations were performed to examine the mechanism of S4 Z movement and gating charge saturation at positive V_m. Residue-residue interactions were also analyzed to understand the atomistic interactions that govern IKs gating. The following sections corroborate the model's ability to simulate both the functional and structural changes of the IKs ion-channel during gating.

3.1: Simulated Single Ion-channel Functional Analysis

The main text (Figure 3) shows simulated single-channel characteristics and its comparison to experiment (77). Other single-channel functional statistics, including latency to first opening, probability of 1st opening, total dwell time and mean open time, calculated from the simulated traces at different V_m are provided in this sub-section. The statistics were tabulated based on discrete SC levels (main text, Figure 2B). Structures with the highest conductance have high Avg.S4Z position (average Z position; over 4 VS in the tetramer) and large pore diameter (PD) as compared to other structures. The total dwell time averaged over 1000 traces showed high SC levels were accessed for longer periods with

increased V_m. Mean open times show that at 80mV, the ion-channel resides for long periods of time at the highest SC level, similar to 60mV, resulting in larger current. Using a threshold of 0.5pA, the latency to first opening was calculated for different membrane potentials. At 60mV, the latency value of 1.65 ± 0.08 seconds is very similar to the experimentally measured value of 1.67± 0.008 seconds. The latency to 1st opening decreased with increased V_m, as expected. The probability of 1st opening at different SC levels increased with time, also as expected. With increased V_m, the ion-channel is more likely to open earlier, as shown in Figure S16.

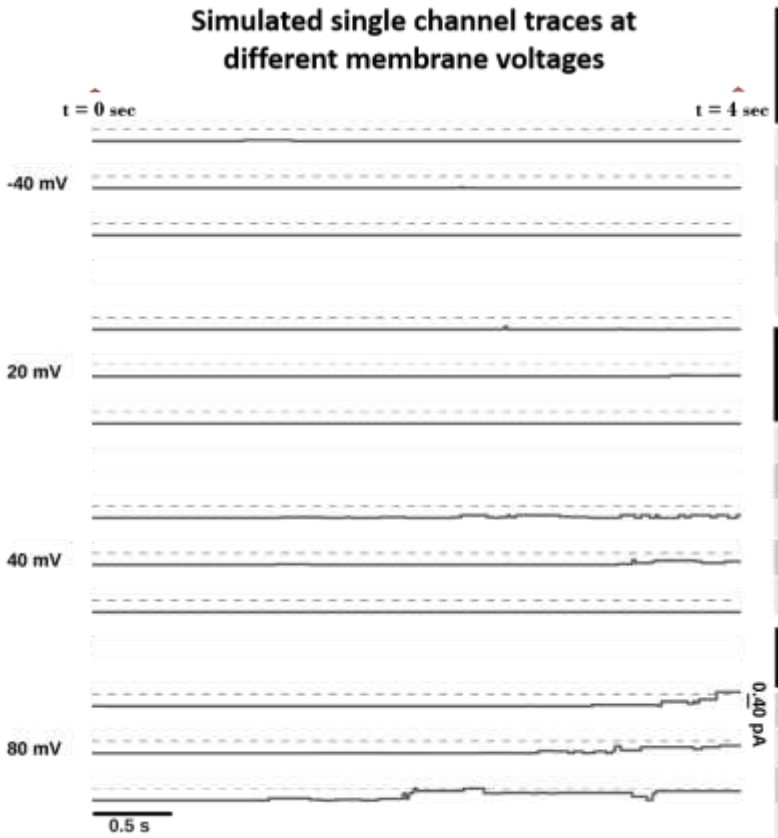

Membrane Voltage	Total Dwell Times (average over 1000 single channel traces; seconds)				
	I	II	III	IV	V
-40 mV	0.183	0.398	0.700	0.139	0.024
20 mV	0.176	0.453	0.715	0.138	0.019
40 mV	0.183	0.415	0.730	0.194	0.095
60 mV	0.206	0.436	0.712	0.344	0.081
80 mV	0.197	0.474	0.738	0.346	0.089

Membrane Voltage	Mean Open Times (1000 single channel traces; seconds)					
	I	II	III	IV	V	Total
-40 mV	0.089	0.097	0.093	0.027	0.080	0.386
20 mV	0.074	0.095	0.093	0.099	0.087	0.448
40 mV	0.079	0.086	0.094	0.085	0.090	0.434
60 mV	0.087	0.076	0.087	0.098	0.116	0.464
80 mV	0.075	0.089	0.081	0.091	0.176	0.512

Membrane Voltage	Latency to 1st Opening (threshold 0.5pA; seconds)
-40 mV	-
20 mV	-
40 mV	2.67 ± 0.01
60 mV	1.65 ± 0.08
80 mV	1.77 ± 0.01

I (0.93-1.4pS) II (1.4-2.07pS) III (2.07-3.14pS) IV (3.14-4.7pS) V (4.7-5.4pS) Total = I+II+III +IV+V

Figure S15. Single-channel Statistics. *(**Left**) Single-channel traces simulated at different depolarizing* V_m *from a holding potential of -80mV for 4 seconds. (**Right**) Table of the total dwell time, mean open time, and latency to 1st opening, for 1000 simulated single-channel traces (examples shown in the left panel). The temporal resolution of the calculations is 0.018 msec. The discrete subconductances used to classify the calculations are*

obtained from main text, Figure 2B. The corresponding SC range of each discrete level is shown in the bottom-right of the figure. (V_m, membrane voltage; SC, subconductance)

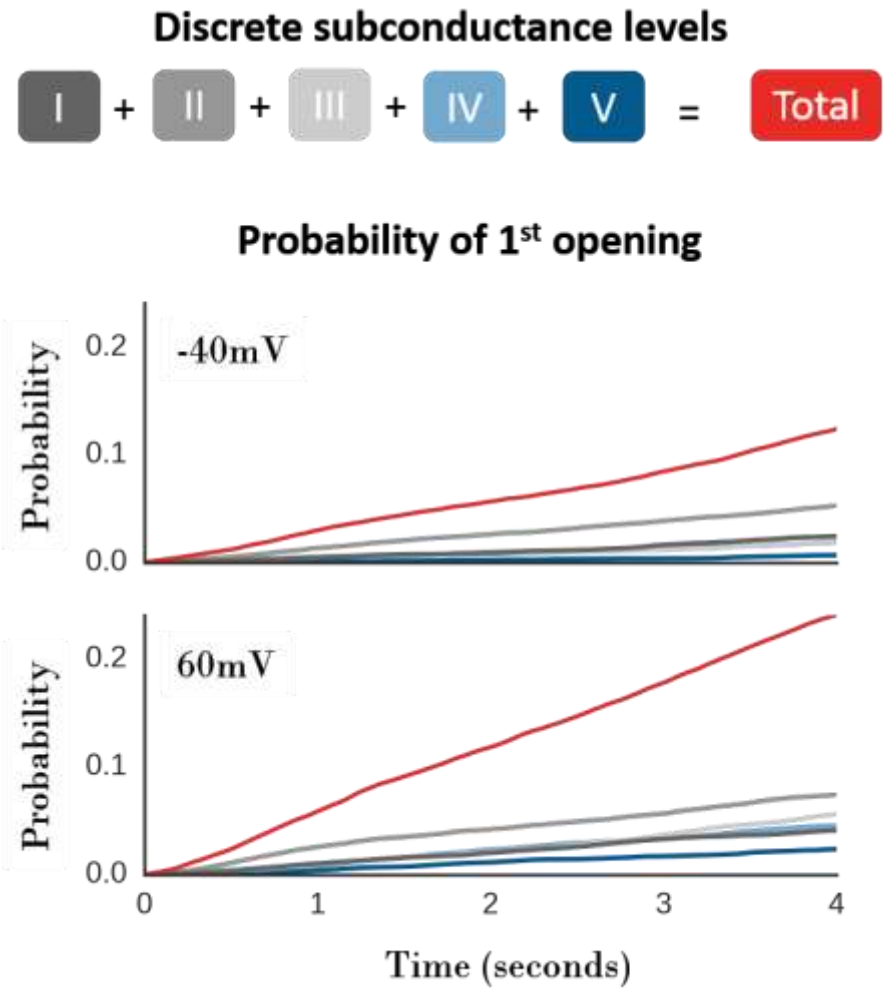

Figure S16. Probability of 1st opening. *The Probability of 1st opening is shown for each discrete SC level for a step depolarization to -40mV (**top**) and 60mV (**bottom**) from a holding potential of -80mV. The probability of 1st opening increases faster at all SC levels for a depolarizing voltage of 60mV as compared to -40mV. The calculations were performed based on discrete SC levels identified in main text, Figure 2B. The probability traces are color coded by SC level (shown on top; total conductance shown in red). (SC, subconductance)*

3.2: Residue Interactions that Govern IKs Gating (Voltage Sensor Movements)

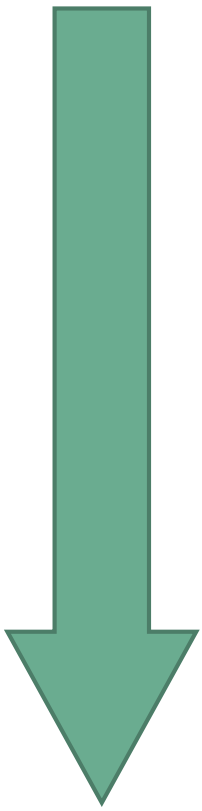

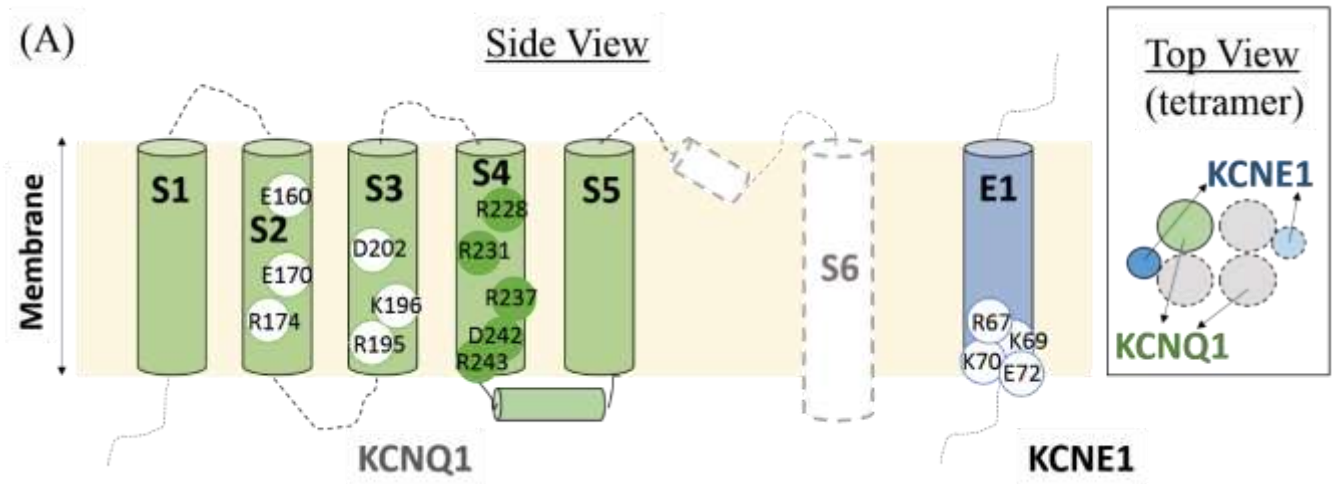
(A)
Side View
Membrane
S1
S2
E160
E170
R174
S3
D202
K196
R195
S4
R228
R231
R237
D242
R243
S5
S6
E1
R67
K69
K70
E72
KCNQ1
KCNE1
Top View
(tetramer)
KCNE1
KCNQ1

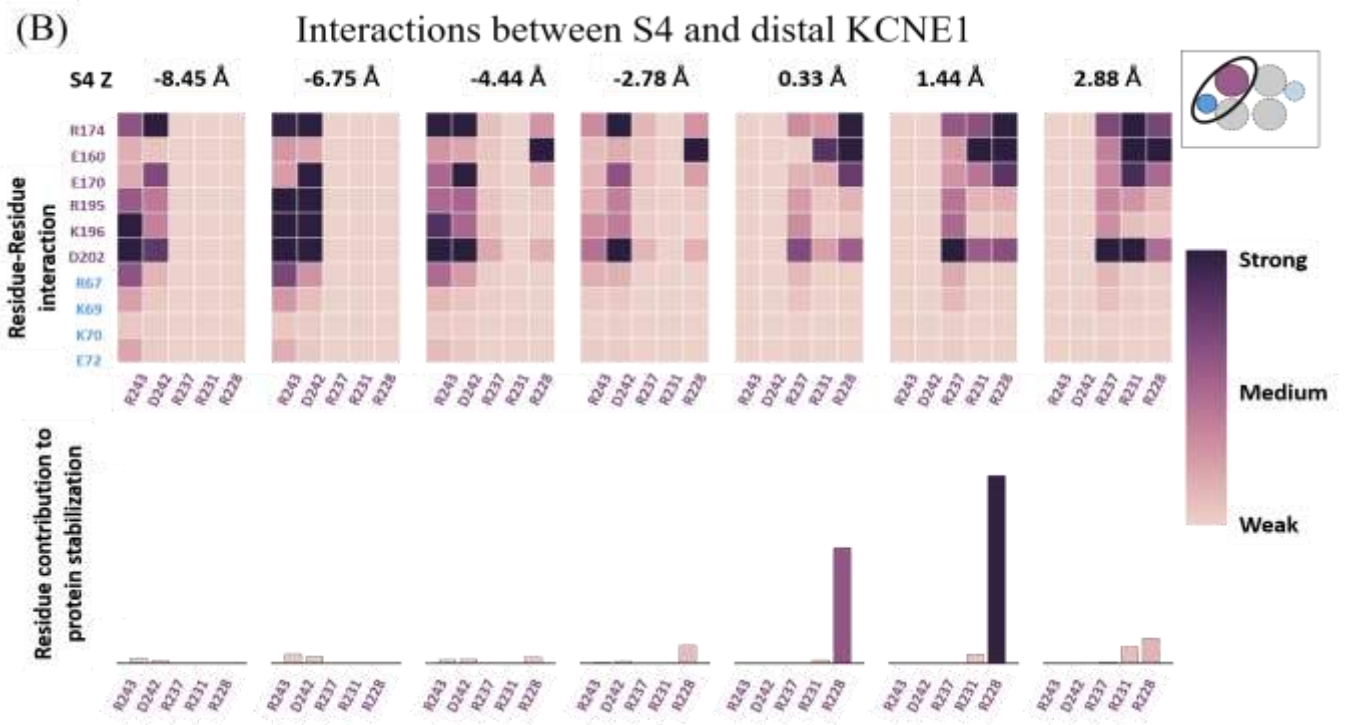
(B)
Interactions between S4 and distal KCNE1
S4 Z
-8.45 Å
-6.75 Å
-4.44 Å
-2.78 Å
0.33 Å
1.44 Å
2.88 Å
Residue-Residue interaction
R174
E160
E170
R195
K196
D202
R67
K69
K70
E72
R243
D242
R237
R231
R228
Strong
Medium
Weak
Residue contribution to protein stabilization

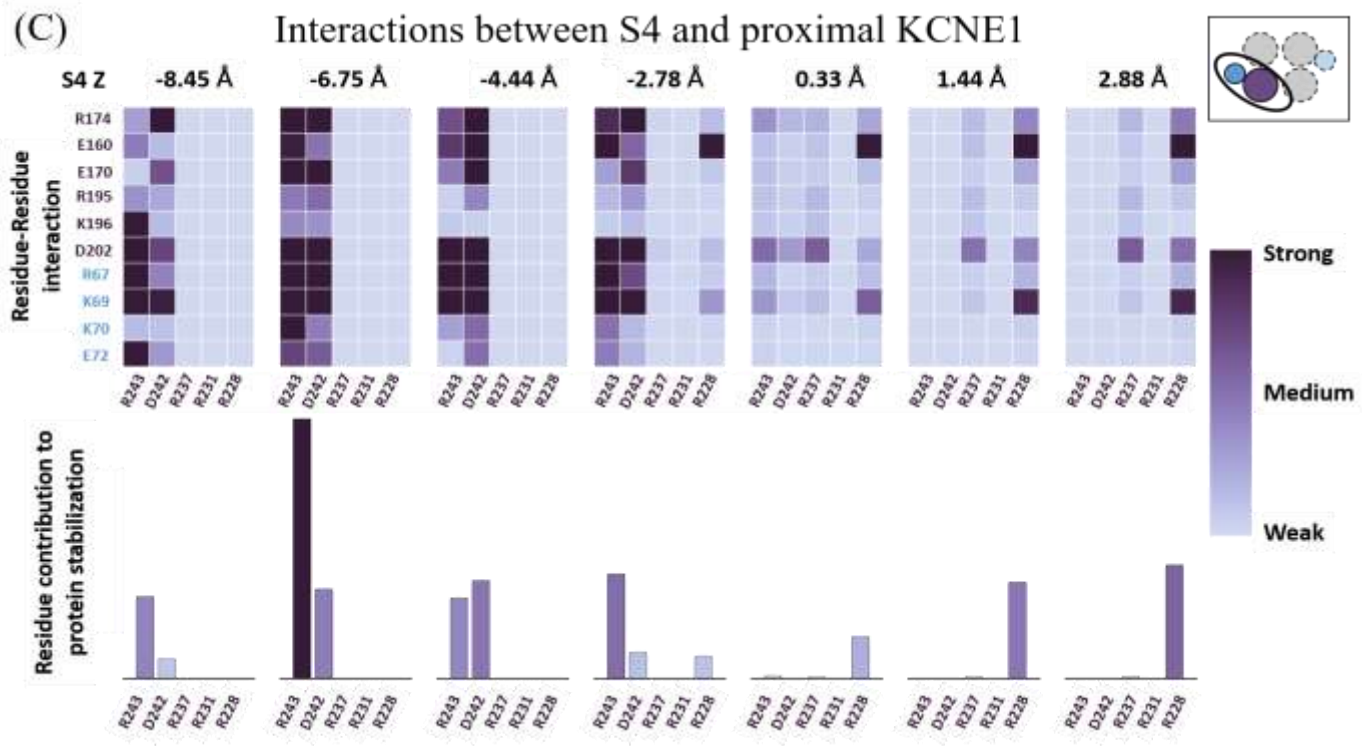

Figure S17. Residue-residue interactions that govern S4 movement in the Z direction at 60mV membrane voltage. ***A***: *Cartoon schema of important charged residues in a single KCNQ1 VSD and a corresponding KCNE1 transmembrane segment. These residues are used in the interaction energy calculations shown in panel B and C. Note that the S4 residues and the KCNE1 segment residues are identified in green (filled circles) and blue (empty circles), respectively. The top view of the KCNQ1 and KCNE1 segments is shown on the right and identically used in (B) and (C) to identify the S4-VSD (KCNQ1) and KCNE1 segments analyzed. The shaded circles with a continuous black outline represent the VSD (green) and KCNE1 (blue) of interest. This basic color scheme*

was used to distinguish S4 residues from other residues in the VSD of interest and also from the KCNE1 residues/segment. Note that the same KCNE1 residues are used in panels B and C energy calculations. ***B: S4 and distal KCNE1****. VSD and S4 residues used in this panel calculations are from the same KCNQ1 segment (identified by color in the inset; shaded pink with a continuous black outline.) The distal KCNE1 residues (inset, shaded blue with continuous black outline) were included in the calculations (the interacting segments are identified by a black oval). The top panel shows the strength of the interactions between S4 residues (pink, x-axis) with other residues within the VSD (pink, y-axis) and the KCNE1 segment (blue, y-axis). The residue-residue interactions were analyzed for different structures at different S4 Z positions (labeled on top of the respective panel) at 60mV membrane potential. The bottom panel shows the relative magnitude of each S4 residue contribution to protein stabilization (favorable interaction strength) corresponding to the top panel. The color-bar representing the strength of the interaction and the residue contribution to total protein energy is displayed on the right.* ***C: S4 and proximal KCNE1****. Similar calculations as in B, are performed with S4 residues and VSD (purple) proximal to the KCNE1 segment (blue); the interacting segments are identified with a black oval in the inset. Same format as panel B. (VSD, Voltage sensor domain)*

3.3: Additional Validation: Subconductances estimated directly from experiments (figure)

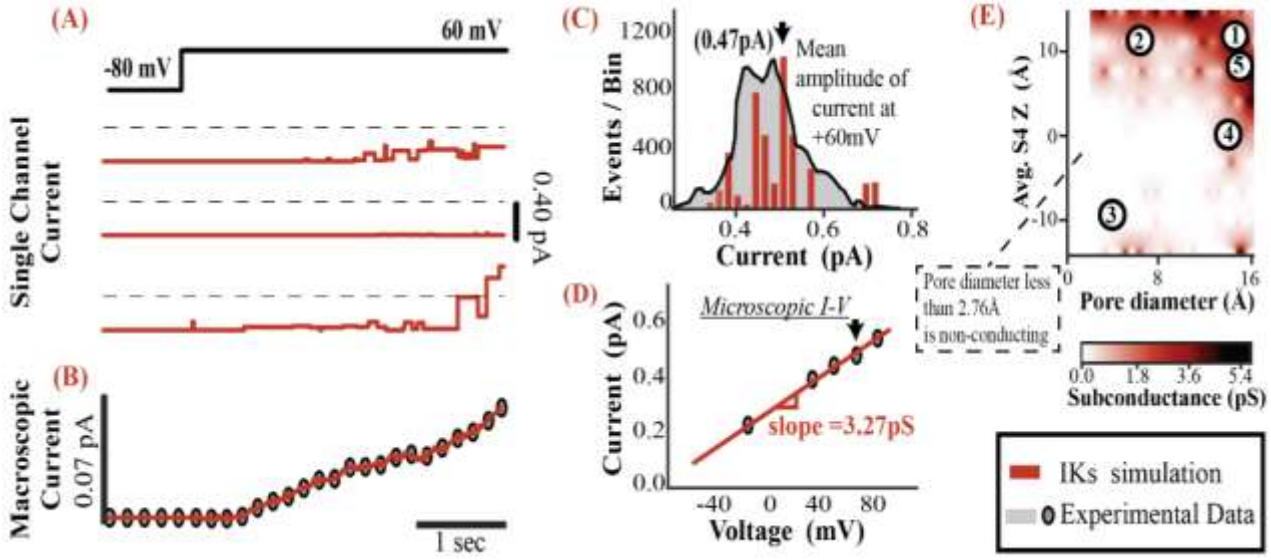

Figure S18. Model-based subconductance estimates using experimental data.

(A) Three of 100 simulated single-channel current traces for a step depolarizing voltage protocol from -80 to 60mV for 4 seconds. (B) The ensemble current (macroscopic, average of 100 traces) fits the experimental data (77) (C) Current amplitude histogram (red) of the simulated single-channel traces (at 60mV, mean amplitude of 0.47pA) and the corresponding experimental data (shaded grey,(77)). The arrow indicates the mean of the current amplitude histogram used in panel D at 60mV (similar arrow). Similar histograms are constructed for a range of V_m to obtain the microscopic I-V relationship in panel D. (D) The simulated mean current amplitude of single-channel traces for several V_m (red line) fits the experimental data (symbols) with a slope (mean conductance) =3.2pS as determined experimentally. (E) SC Map, estimated from purely

experimental data, projected onto two structural dimensions - PD and Avg.S4Z (77). The numbers refer to the structures in main text, Figure 2B. The legend for panels A-D is shown on the bottom right of the figure. Pore diameter less than 2.76Å (smaller than K^+ ion) is considered to be non-conducting. (pS, pico-Siemens (10e-12 Siemens)

References

1. Haitin, Y., R. Wiener, D. Shaham, A. Peretz, E.B.-T. Cohen, L. Shamgar, O. Pongs, J.A. Hirsch, and B. Attali. 2009. Intracellular domains interactions and gated motions of IKS potassium channel subunits. EMBO J. 28: 1994–2005.

2. Wiener, R., Y. Haitin, L. Shamgar, M.C. Fernández-Alonso, A. Martos, O. Chomsky-Hecht, G. Rivas, B. Attali, and J.A. Hirsch. 2008. The KCNQ1 (Kv7.1) COOH Terminus, a Multitiered Scaffold for Subunit Assembly and Protein Interaction. J. Biol. Chem. 283: 5815–5830.

3. Kang, C., C. Tian, F.D. Sönnichsen, J.A. Smith, J. Meiler, A.L. George, C.G. Vanoye, H.J. Kim, and C.R. Sanders. 2008. Structure of KCNE1 and Implications for How It Modulates the KCNQ1 Potassium Channel†‡. Biochemistry (Mosc.). 47: 7999–8006.

4. Du, L.-P., M.-Y. Li, K.-C. Tsai, Q.-D. You, and L. Xia. 2005. Characterization of binding site of closed-state KCNQ1 potassium channel by homology modeling, molecular docking, and pharmacophore identification. Biochem. Biophys. Res. Commun. 332: 677–687.

5. Van Horn, W.D., C.G. Vanoye, and C.R. Sanders. Working model for the structural basis for KCNE1 modulation of the KCNQ1 potassium channel. Curr. Opin. Struct. Biol. In Press, Corrected Proof.

6. Silva, J.R., H. Pan, D. Wu, A. Nekouzadeh, K.F. Decker, J. Cui, N.A. Baker, D. Sept, and Y. Rudy. 2009. A multiscale model linking ion-channel molecular dynamics and electrostatics to the cardiac action potential. Proc. Natl. Acad. Sci. 106: 11102–11106.

7. Nekouzadeh, A., and Y. Rudy. 2011. Continuum Molecular Simulation of Large Conformational Changes during Ion–Channel Gating. PLoS ONE. 6: e20186.

8. Long, S.B., X. Tao, E.B. Campbell, and R. MacKinnon. 2007. Atomic structure of a voltage-dependent K+ channel in a lipid membrane-like environment. Nature. 450: 376–382.

9. Yarov-Yarovoy, V., D. Baker, and W.A. Catterall. 2006. Voltage sensor conformations in the open and closed states in ROSETTA structural models of K(+) channels. Proc. Natl. Acad. Sci. U. S. A. 103: 7292–7297.

10. Rohl, C.A., C.E.M. Strauss, D. Chivian, and D. Baker. 2004. Modeling structurally variable regions in homologous proteins with rosetta. Proteins. 55: 656–677.

11. Sun, J., and R. MacKinnon. 2017. Cryo-EM Structure of a KCNQ1/CaM Complex Reveals Insights into Congenital Long QT Syndrome. Cell. 169: 1042-1050.e9.

12. Jespersen, T., M. Membrez, C.S. Nicolas, B. Pitard, O. Staub, S.-P. Olesen, I. Baró, and H. Abriel. 2007. The KCNQ1 potassium channel is down-regulated by ubiquitylating enzymes of the Nedd4/Nedd4-like family. Cardiovasc. Res. 74: 64–74.

13. Tian, C., C.G. Vanoye, C. Kang, R.C. Welch, H.J. Kim, A.L. George Jr, and C.R. Sanders. 2007. Preparation, functional characterization, and NMR studies of human KCNE1, a voltage-gated potassium channel accessory subunit associated with deafness and long QT syndrome. Biochemistry (Mosc.). 46: 11459–11472.

14. Sahu, I.D., B.M. Kroncke, R. Zhang, M.M. Dunagan, H.J. Smith, A. Craig, R.M. McCarrick, C.R. Sanders, and G.A. Lorigan. 2014. Structural investigation of the transmembrane domain of KCNE1 in proteoliposomes. Biochemistry (Mosc.). 53: 6392–6401.

15. Sahu, I.D., A.F. Craig, M.M. Dunagan, K.R. Troxel, R. Zhang, A.G. Meiberg, C.N. Harmon, R.M. McCarrick, B.M. Kroncke, C.R. Sanders, and G.A. Lorigan. 2015. Probing Structural Dynamics and Topology of the KCNE1 Membrane Protein in Lipid Bilayers via Site-Directed Spin Labeling and Electron Paramagnetic Resonance Spectroscopy. Biochemistry (Mosc.). 54: 6402–6412.

16. Zhang Rongfu, Sahu Indra D., Gibson Kaylee R., Muhammad Nefertiti B., Bali Avnika P., Comer Raven G., Liu Lishan, Craig Andrew F., Mccarrick Robert M., Dabney-Smith Carole, Sanders Charles R., and Lorigan Gary A. 2015. Development of electron spin echo envelope modulation spectroscopy to probe the secondary structure of recombinant membrane proteins in a lipid bilayer. Protein Sci. 24: 1707–1713.

17. Raveh, B., N. London, and O. Schueler-Furman. 2010. Sub-angstrom modeling of complexes between flexible peptides and globular proteins. Proteins. 78: 2029–2040.

18. Jalily Hasani, H., M. Ahmed, and K. Barakat. 2017. A comprehensive structural model for the human KCNQ1/KCNE1 ion channel. J. Mol. Graph. Model. 78: 26–47.

19. Sachyani, D., M. Dvir, R. Strulovich, G. Tria, W. Tobelaim, A. Peretz, O. Pongs, D. Svergun, B. Attali, and J.A. Hirsch. 2014. Structural Basis of a Kv7.1 Potassium Channel Gating Module: Studies of the Intracellular C-Terminal Domain in Complex with Calmodulin. Structure. 22: 1582–1594.

20. Shamgar, L., L. Ma, N. Schmitt, Y. Haitin, A. Peretz, R. Wiener, J. Hirsch, O. Pongs, and B. Attali. 2006. Calmodulin Is Essential for Cardiac IKS Channel Gating and Assembly: Impaired Function in Long-QT Mutations. Circ Res. 98: 1055–1063.

21. Chung, H.J. 2014. Role of calmodulin in neuronal Kv7/KCNQ potassium channels and epilepsy. Front. Biol. : 1–11.

22. Gamper, N., Y. Li, and M.S. Shapiro. 2005. Structural Requirements for Differential Sensitivity of KCNQ K+ Channels to Modulation by Ca2+/Calmodulin. Mol Biol Cell. 16: 3538–3551.

23. Touw, W.G., C. Baakman, J. Black, T.A.H. te Beek, E. Krieger, R.P. Joosten, and G. Vriend. 2015. A series of PDB-related databanks for everyday needs. Nucleic Acids Res. 43: D364–D368.

24. Kabsch, W., and C. Sander. 1983. Dictionary of protein secondary structure: pattern recognition of hydrogen-bonded and geometrical features. Biopolymers. 22: 2577–2637.

25. Haitin, Y., and B. Attali. 2008. The C-terminus of Kv7 channels: a multifunctional module. J. Physiol. 586: 1803–1810.

26. Kaufmann, K.W., G.H. Lemmon, S.L. DeLuca, J.H. Sheehan, and J. Meiler. 2010. Practically Useful: What the Rosetta Protein Modeling Suite Can Do for You. Biochemistry (Mosc.). 49: 2987–2998.

27. Chen, J., R. Zheng, Y.F. Melman, and T.V. McDonald. Functional Interactions between KCNE1 C-Terminus and the KCNQ1 Channel. PLoS ONE. 4: e5143.

28. Raveh, B., N. London, L. Zimmerman, and O. Schueler-Furman. 2011. Rosetta FlexPepDock ab-initio: Simultaneous Folding, Docking and Refinement of Peptides onto Their Receptors. PLoS ONE. 6: e18934.

29. Webb, B., and A. Sali. 2014. Protein structure modeling with MODELLER. Methods Mol. Biol. Clifton NJ. 1137: 1–15.

30. Nakajo, K., M.H. Ulbrich, Y. Kubo, and E.Y. Isacoff. 2010. Stoichiometry of the KCNQ1 - KCNE1 ion channel complex. Proc. Natl. Acad. Sci. 107: 18862–18867.

31. Nakajo, K., M.H. Ulbrich, Y. Kubo, and E.Y. Isacoff. 2010. Stoichiometry of KCNQ1-KCNE1 Ion Channel Complex is Flexible and Density-Dependent. Biophys. J. 98: 136a-137a.

32. Wang, K., C. Terrenoire, K.J. Sampson, V. Iyer, J.D. Osteen, J. Lu, G. Keller, D.N. Kotton, and R.S. Kass. 2011. Biophysical properties of slow potassium channels in human embryonic stem cell derived cardiomyocytes implicate subunit stoichiometry. J. Physiol. 589: 6093–6104.

33. Yu, H., Z. Lin, M.E. Mattmann, B. Zou, C. Terrenoire, H. Zhang, M. Wu, O.B. McManus, R.S. Kass, C.W. Lindsley, C.R. Hopkins, and M. Li. 2013. Dynamic subunit stoichiometry confers a progressive continuum of pharmacological sensitivity by KCNQ potassium channels. Proc. Natl. Acad. Sci. 110: 8732-8737.

34. Murray, C.I., M. Westhoff, J. Eldstrom, E. Thompson, R. Emes, and D. Fedida. 2016. Unnatural amino acid photo-crosslinking of the IKs channel complex demonstrates a KCNE1:KCNQ1 stoichiometry of up to 4:4. eLife. : e11815.

35. Baker, O.S., H.P. Larsson, L.M. Mannuzzu, and E.Y. Isacoff. 1998. Three Transmembrane Conformations and Sequence-Dependent Displacement of the S4 Domain in Shaker K+ Channel Gating. Neuron. 20: 1283–1294.

36. Ruta, V., J. Chen, and R. MacKinnon. 2005. Calibrated Measurement of Gating-Charge Arginine Displacement in the KvAP Voltage-Dependent K+ Channel. Cell. 123: 463–475.

37. Posson, D.J., P. Ge, C. Miller, F. Bezanilla, and P.R. Selvin. 2005. Small vertical movement of a K+ channel voltage sensor measured with luminescence energy transfer. Nature. 436: 848–851.

38. Long, S.B., E.B. Campbell, and R. MacKinnon. 2005. Crystal Structure of a Mammalian Voltage-Dependent Shaker Family K+ Channel. Science. 309: 897–903.

39. Tombola, F., M.M. Pathak, and E.Y. Isacoff. 2006. How Does Voltage Open an Ion Channel? Annu. Rev. Cell Dev. Biol. 22: 23–52.

40. Kalstrup, T., and R. Blunck. 2016. Probing the S4-S5 Linker Movement During Activation in KV Channels. Biophys. J. 110: 104a.

41. Börjesson, S.I., and F. Elinder. 2008. Structure, Function, and Modification of the Voltage Sensor in Voltage-Gated Ion Channels. Cell Biochem. Biophys. 52: 149–174.

42. Haitin, Y., I. Yisharel, E. Malka, L. Shamgar, H. Schottelndreier, A. Peretz, Y. Paas, and B. Attali. 2008. S1 Constrains S4 in the Voltage Sensor Domain of Kv7.1 K+ Channels. PLOS ONE. 3: e1935.

43. Rocheleau, J.M., and W.R. Kobertz. 2008. KCNE Peptides Differently Affect Voltage Sensor Equilibrium and Equilibration Rates in KCNQ1 K+ Channels. J. Gen. Physiol. 131: 59–68.

44. Lvov, A., S.D. Gage, V.M. Berrios, and W.R. Kobertz. 2010. Identification of a protein–protein interaction between KCNE1 and the activation gate machinery of KCNQ1. J. Gen. Physiol. 135: 607–618.

45. Wu, D., K. Delaloye, M.A. Zaydman, A. Nekouzadeh, Y. Rudy, and J. Cui. 2010. State-dependent electrostatic interactions of S4 arginines with E1 in S2 during Kv7.1 activation. J. Gen. Physiol. 135: 595–606.

46. Ma, L.-J., I. Ohmert, and V. Vardanyan. 2011. Allosteric Features of KCNQ1 Gating Revealed by Alanine Scanning Mutagenesis. Biophys. J. 100: 885–894.

47. Ruscic, K.J., F. Miceli, C.A. Villalba-Galea, H. Dai, Y. Mishina, F. Bezanilla, and S.A.N. Goldstein. 2013. IKs channels open slowly because KCNE1 accessory subunits slow the movement of S4 voltage sensors in KCNQ1 pore-forming subunits. Proc. Natl. Acad. Sci. 110: E559–E566.

48. Eckey, K., E. Wrobel, G. Seebohm, L. Pott, N. Schmitt, and N. Strutz-Seebohm. 2014. Novel Kv7.1-phosphatidylinositol 4,5-bisphosphate (PIP2) interaction sites uncovered by charge neutralization scanning. J. Biol. Chem. : jbc.M114.589796.

49. Kleiger, G., A. Saha, S. Lewis, B. Kuhlman, and R.J. Deshaies. 2009. Rapid E2-E3 assembly and disassembly enable processive ubiquitylation of cullin-RING ubiquitin ligase substrates. Cell. 139: 957–968.

50. Callenberg, K.M., O.P. Choudhary, G.L. de Forest, D.W. Gohara, N.A. Baker, and M. Grabe. 2010. APBSmem: A Graphical Interface for Electrostatic Calculations at the Membrane. PLoS ONE. 5: e12722.

51. Dolinsky, T.J., J.E. Nielsen, J.A. McCammon, and N.A. Baker. 2004. PDB2PQR: an automated pipeline for the setup of Poisson–Boltzmann electrostatics calculations. Nucleic Acids Res. 32: W665–W667.

52. Dolinsky, T.J., P. Czodrowski, H. Li, J.E. Nielsen, J.H. Jensen, G. Klebe, and N.A. Baker. 2007. PDB2PQR: expanding and upgrading automated preparation of biomolecular structures for molecular simulations. Nucleic Acids Res. 35: W522–W525.

53. Bank, R., and M. Holst. 2003. A New Paradigm for Parallel Adaptive Meshing Algorithms. SIAM Rev. 45: 291–323.

54. Holst, M. 2001. Adaptive Numerical Treatment of Elliptic Systems on Manifolds. Adv. Comput. Math. 15: 139–191.

55. Prusinkiewicz, P., and A. Lindenmayer. 1990. The algorithmic beauty of plants. New York: Springer-Verlag.

56. Jaillet, L., A. Yershova, S.M. La Valle, and T. Siméon. 2005. Adaptive tuning of the sampling domain for dynamic-domain RRTs. In: 2005 IEEE/RSJ International Conference on Intelligent Robots and Systems. IEEE. pp. 2851–2856.

57. Yershova, A., and S.M. LaValle. 2007. Improving motion-planning algorithms by efficient nearest-neighbor searching. IEEE Trans. Robot. 23: 151–157.

58. Zhong, J., and J. Su. 2012. Triple-Rrts for robot path planning based on narrow passage identification. In: 2012 International Conference on Computer Science and Information Processing (CSIP). pp. 188–192.

59. Yershova, A., and S.M. LaValle. 2009. Motion Planning for Highly Constrained Spaces. In: Robot Motion and Control 2009. Springer, London. pp. 297–306.

60. Nekouzadeh, A., and Y. Rudy. 2016. Conformational changes of an ion-channel during gating and emerging electrophysiologic properties: Application of a computational approach to cardiac Kv7.1. Prog. Biophys. Mol. Biol. 120: 18–27.

61. Broomand, A., and F. Elinder. 2008. Large-Scale Movement within the Voltage-Sensor Paddle of a Potassium Channel—Support for a Helical-Screw Motion. Neuron. 59: 770–777.

62. Jiang, Y., V. Ruta, J. Chen, A. Lee, and R. MacKinnon. 2003. The principle of gating charge movement in a voltage-dependent K+ channel. Nature. 423: 42–48.

63. Hackos, D.H., T.-H. Chang, and K.J. Swartz. 2002. Scanning the Intracellular S6 Activation Gate in the Shaker K+ Channel. J. Gen. Physiol. 119: 521–531.

64. Phillips James C., Braun Rosemary, Wang Wei, Gumbart James, Tajkhorshid Emad, Villa Elizabeth, Chipot Christophe, Skeel Robert D., Kalé Laxmikant, and Schulten Klaus. 2005. Scalable molecular dynamics with NAMD. J. Comput. Chem. 26: 1781–1802.

65. Humphrey, W., A. Dalke, and K. Schulten. 1996. VMD: visual molecular dynamics. J. Mol. Graph. 14: 33–38, 27–28.

66. Huang, J., S. Rauscher, G. Nawrocki, T. Ran, M. Feig, B.L. de Groot, H. Grubmüller, and A.D. MacKerell Jr. 2017. CHARMM36m: an improved force field for folded and intrinsically disordered proteins. Nat. Methods. 14: 71–73.

67. Baker, N.A., D. Sept, S. Joseph, M.J. Holst, and J.A. McCammon. 2001. Electrostatics of nanosystems: Application to microtubules and the ribosome. Proc. Natl. Acad. Sci. 98: 10037–10041.

68. Breiman, L. 2001. Random Forests. Mach. Learn. 45: 5–32.

69. Buitinck, L., G. Louppe, M. Blondel, F. Pedregosa, A. Mueller, O. Grisel, V. Niculae, P. Prettenhofer, A. Gramfort, J. Grobler, R. Layton, J. Vanderplas, A. Joly, B. Holt, and G. Varoquaux. 2013. API design for machine learning software: experiences from the scikit-learn project. ArXiv13090238 Cs. .

70. Pedregosa, F., G. Varoquaux, A. Gramfort, V. Michel, B. Thirion, O. Grisel, M. Blondel, P. Prettenhofer, R. Weiss, V. Dubourg, J. Vanderplas, A. Passos, D. Cournapeau, M. Brucher, M. Perrot, and É. Duchesnay. 2011. Scikit-learn: Machine Learning in Python. J. Mach. Learn. Res. 12: 2825–2830.

71. Tipping, M.E., and C.M. Bishop. 1999. Probabilistic Principal Component Analysis. J. R. Stat. Soc. Ser. B Stat. Methodol. 61: 611–622.

72. Halko, N., P. Martinsson, and J. Tropp. 2011. Finding Structure with Randomness: Probabilistic Algorithms for Constructing Approximate Matrix Decompositions. SIAM Rev. 53: 217–288.

73. Weiss, Y., and E.H. Adelson. 1995. MIT Media Laboratory Perceptual Computing Section Technical Report No. 344 Motion Estimation and Segmentation Using a Recurrent Mixture of Experts Architecture. In: IEEE Workshop on Neural Network for Signal Processing. Citeseer.

74. Hastings, W.K. 1970. Monte Carlo sampling methods using Markov chains and their applications. Biometrika. 57: 97–109.

75. Gilks, W.R., S. Richardson, and D. Spiegelhalter. 1995. Markov Chain Monte Carlo in Practice. CRC Press.

76. Scherer, M.K., B. Trendelkamp-Schroer, F. Paul, G. Pérez-Hernández, M. Hoffmann, N. Plattner, C. Wehmeyer, J.-H. Prinz, and F. Noé. 2015. PyEMMA 2: A Software Package

for Estimation, Validation, and Analysis of Markov Models. J. Chem. Theory Comput. 11: 5525–5542.

77. Werry, D., J. Eldstrom, Z. Wang, and D. Fedida. 2013. Single-channel basis for the slow activation of the repolarizing cardiac potassium current, IKs. Proc. Natl. Acad. Sci. 110: E996–E1005.

Additional References

Moss AJ, Kass RS (2005) Long QT syndrome: from channels to cardiac arrhythmias. J Clin Invest 115(8):2018–2024.

Chouabe C, et al. (2000) Novel mutations in KvLQT1 that affect Iks activation through interactions with Isk. Cardiovasc Res 45(4):971–980.

Goldman AM, et al. (2009) Arrhythmia in Heart and Brain: KCNQ1 Mutations Link Epilepsy and Sudden Unexplained Death. Sci Transl Med 1(2):2ra6.

Lopez GA, Nung Jan Y, Jan LY (1994) Evidence that the S6 segment of the Shaker voltage-gated K+ channel comprises part of the pore. Nature 367(6459):179–182.

Ding S, Horn R (2002) Tail End of the S6 Segment. J Gen Physiol 120(1):87–97.

Lane TJ, Shukla D, Beauchamp KA, Pande VS (2013) To Milliseconds and Beyond: Challenges in the Simulation of Protein Folding. Curr Opin Struct Biol 23(1):58–65.

Breiman L (2001) Random Forests. Mach Learn 45(1):5–32.

Chapman ML, VanDongen AMJ (2005) K channel subconductance levels result from heteromeric pore conformations. J Gen Physiol 126(2):87–103.

Chapman ML, VanDongen HMA, VanDongen AMJ (1997) Activation-Dependent Subconductance Levels in the drk1 K Channel Suggest a Subunit Basis for Ion Permeation and Gating. Biophys J 72(2):708–719.

Cheneke BR, van den Berg B, Movileanu L (2011) Analysis of Gating Transitions among the Three Major Open States of the OpdK Channel. Biochemistry (Mosc) 50(22):4987–4997.

Zifarelli G, Pusch M (2007) CLC chloride channels and transporters: a biophysical and physiological perspective. Reviews of Physiology, Biochemistry and

Pharmacology, ed Amara SG (Springer Berlin Heidelberg, Berlin, Heidelberg), pp 23–76.

Shieh CC, Kirsch GE (1994) Mutational analysis of ion conduction and drug binding sites in the inner mouth of voltage-gated K+ channels. Biophysical Journal 67(6):2316–2325.

Bezanilla F (2005) The Origin of Subconductance Levels in Voltage-gated K+ Channels. J Gen Physiol 126(2):83–86.

Ruscic KJ, et al. (2013) IKs channels open slowly because KCNE1 accessory subunits slow the movement of S4 voltage sensors in KCNQ1 pore-forming subunits. Proc Natl Acad Sci 110(7):E559–E566.

Nakajo K, Kubo Y (2014) Steric hindrance between S4 and S5 of the KCNQ1/KCNE1 channel hampers pore opening. Nat Commun 5. doi:10.1038/ncomms5100.

Gagnon DG, Bezanilla F (2010) The contribution of individual subunits to the coupling of the voltage sensor to pore opening in Shaker K channels: effect of ILT mutations in heterotetramers. J Gen Physiol 136(5):555–568.

Horn R, Ding S, Gruber HJ (2000) Immobilizing the moving parts of voltage-gated ion channels. J Gen Physiol 116(3):461–476.

Ledwell JL, Aldrich RW (1999) Mutations in the S4 region isolate the final voltage-dependent cooperative step in potassium channel activation. J Gen Physiol 113(3):389–414.

Pathak M, Kurtz L, Tombola F, Isacoff E (2005) The Cooperative Voltage Sensor Motion that Gates a Potassium Channel. J Gen Physiol 125(1):57–69.

Yifrach O, Zandany N, Shem-Ad T (2009) Examining cooperative gating phenomena in voltage-dependent potassium channels: taking the energetic approach. Methods Enzymol 466:179–209.

Zagotta WN, Hoshi T, Aldrich RW (1994) Shaker potassium channel gating. III: Evaluation of kinetic models for activation. J Gen Physiol 103(2):321–362.

Gilks WR, Richardson S, Spiegelhalter D (1995) Markov Chain Monte Carlo in Practice (CRC Press).

Brest J, Zumer V, Maucec MS (2006) Self-Adaptive Differential Evolution Algorithm in Constrained Real-Parameter Optimization. 2006 IEEE International Conference on Evolutionary Computation, pp 215–222.